

# The Population of Tiny Near-Earth Objects Observed by NEOWISE

A. Mainzer<sup>1</sup>, J. Bauer<sup>1,2</sup>, T. Grav<sup>3</sup>, J. Masiero<sup>1</sup>, R. M. Cutri<sup>2</sup>, E. Wright<sup>4</sup>, C. R. Nugent<sup>1</sup>,  
R. Stevenson<sup>1</sup>, E. Clyne<sup>1</sup>, G. Cukrov<sup>1</sup>, F. Masci<sup>2</sup>

amainzer@jpl.nasa.gov

## ABSTRACT

Only a very small fraction of the asteroid population at size scales comparable to the object that exploded over Chelyabinsk, Russia has been discovered to date, and physical properties are poorly characterized. We present previously unreported detections of 106 close approaching near-Earth objects (NEOs) by the Wide-field Infrared Survey Explorer mission's NEOWISE project. These infrared observations constrain physical properties such as diameter and albedo for these objects, many of which are found to be smaller than 100 m. Because these objects are intrinsically faint, they were detected by WISE during very close approaches to the Earth, often at large apparent on-sky velocities. We observe a trend of increasing albedo with decreasing size, but as this sample of NEOs was discovered by visible light surveys, it is likely that selection biases against finding small, dark NEOs influence this finding.

## 1. Introduction

As the products of collisional processes, small near-Earth objects (NEOs), defined as minor planets with perihelia less than 1.3 AU, are far more numerous than larger ones. Discovering, tracking, and characterizing these objects allows us to better understand the

---

<sup>1</sup>Jet Propulsion Laboratory, California Institute of Technology, Pasadena, CA 91109 USA

<sup>2</sup>Infrared Processing and Analysis Center, California Institute of Technology, Pasadena, CA 91125, USA

<sup>3</sup>Planetary Science Institute, Tucson, AZ USA

<sup>4</sup>Department of Physics and Astronomy, UCLA, PO Box 91547, Los Angeles, CA 90095-1547 USA

impact hazard they pose to Earth, as well as their origins and subsequent evolution. Because their small sizes usually make them undetectable until they are very nearby the Earth, it is often difficult for the current suite of asteroid surveys and follow-up telescopes to track them for very long. Consequently, the fraction of the total population at small sizes that has been discovered to date remains very low. While about 90% of NEOs with effective spherical diameters larger than 1 km have now been discovered, the integral survey completeness drops to  $\sim 25\%$  at 100 m, and it is likely to be  $< 1\%$  at sizes comparable to the 17-20 m diameter NEO that exploded over Chelyabinsk, Russia on February 15, 2013 (Mainzer et al. 2011a; Harris 2008).

Approximately 10,000 NEOs have been discovered to date,  $\sim 900$  of which are 1 km or larger. The current catalog includes  $\sim 3500$  objects with absolute magnitude  $H > 22.75$  mag. This corresponds to a diameter of 100 m or smaller assuming a geometric visible albedo  $p_V$  of 14%, the average albedo for the infrared-selected NEO sample from Mainzer et al. (2011a), using the relationship

$$D = \left[ \frac{1329 \cdot 10^{-0.2H}}{p_V^{1/2}} \right], \quad (1)$$

where  $D$  is the effective spherical diameter (Fowler & Chillemi 1992; Bowell et al. 1989). For NEOs with diameters less than 20 m, corresponding to  $H > 26.25$  mag for  $p_V = 14\%$ , there are  $\sim 720$  objects that have been discovered to date. However, the true number is quite uncertain, since NEO albedos are known to range from  $\sim 1\%$  to  $> 50\%$  (Mainzer et al. 2011a; Trilling et al. 2010; Stuart & Binzel 2004). For NEOs 10 m and smaller, it is reasonable to assume that somewhere between 50 - 150 have been discovered. The true numbers discovered at different size ranges depend on the objects' albedos, of course, and it is not possible to extrapolate the sample of discovered objects to the entire population without careful accounting for survey biases due to instrument sensitivity, survey cadence, weather, seeing, availability of follow-up assets, etc. (c.f. Jedicke & Metcalfe 1998; Spahr 1998; Bottke et al. 2002; Mainzer et al. 2011a, 2012c; Grav et al. 2011, 2012a). At these very small sizes, the survey completeness is very low.

Given recent interest in NEOs down to even very small sizes, it is useful to compute the average albedo for tiny NEOs discovered by visible light surveys and see how it compares to the average albedo determined for NEOs larger than 100 m by the sample returned by the *Wide-field Infrared Survey Explorer's* NEOWISE project (Wright et al. 2010; Mainzer et al. 2011a,b). Because NEOWISE detected and discovered NEOs using thermal infrared wavelengths, and because new discoveries received timely ground-based follow-up, its sample was shown to be essentially albedo-insensitive (Mainzer et al. 2011a). The average albedo found by that sample was 14% for NEOs 100 m and larger. Few objects smaller than 100 m were detected by the NEOWISE automated minor planet detection software, known as the

WISE Moving Object Processing System (WMOPS), which required five or more detections of objects moving at apparent on-sky velocities slower than  $\sim 3.2^\circ/\text{day}$ . In general, NEOs smaller than  $\sim 100$  m are only detected when they are quite close, resulting in significantly higher angular velocities; the smallest objects, with sizes  $< 10$  m, were detected when they were only 2-3 lunar distances away from Earth. Such small objects often passed through the WISE field of view fewer than the five times required for WMOPS to detect them. Alternately, they may have passed through the field of view more than five times, but were too faint to have been detected at least five times because of their small size or because they were trailed in the individual exposures.

A total of 429 NEOs detected by WMOPS were reported from the fully cryogenic portion of the survey, and 116 NEOs were detected and/or discovered following the partial and complete depletion of the spacecraft’s cryogen (Mainzer et al. 2011a, 2012b). All but a handful were larger than 100 m. Here, we report the detection by NEOWISE of an additional 106 NEOs that were discovered by ground-based visible light surveys and made very close approaches to the Earth while WISE was observing. These objects tend to be small and fast-moving. This sample represents a pilot study for a future effort to conduct a wholesale search of the NEOWISE databases and images for the entire set of known minor planets; this effort will be carried out by the NEOWISE project in the near future.

## 2. Methods

A combination of methods were used to identify known objects that were not previously identified by WMOPS in the single-exposure images. Images were searched using the Infrared Science Archive (IRSA)/WISE Image Service<sup>1</sup> as well as by searching the WISE single-exposure source database using the Known Solar System Object Possible Association List (KSSOPAL; Cutri et al. 2012). Both of these tools compute an object’s ephemeris and predict where it would have intersected with a WISE observation. While WMOPS actively rejects stationary objects such as stars and galaxies before linking transient detections, neither the Image Service nor KSSOPAL discriminates between stationary objects and the asteroid, so the probability of a chance association is greater. We rejected stationary objects by examining the WISE Atlas Images and Catalogs, which combine all possible exposures at a given location to produce a deeper image, following the methods described in Mainzer et al. (2011a,c).

Of the currently known NEOs with  $H > 26.25$  mag, the median observational arc length

---

<sup>1</sup><https://irsa.ipac.caltech.edu/applications/wise/>

spans only  $\sim 3$  days, and only a few dozen exceed 20 days. The vast majority of these objects are therefore lost, frustrating efforts to locate them in the NEOWISE data. However, many of the objects that were discovered by ground-based surveys during the WISE survey phase did pass through the WISE field of view near  $90^\circ$  solar elongation and were bright enough to be detected, albeit often with fewer than five observations. Only those objects whose astrometric uncertainties were very small (less than a few arc seconds) at the time of their passage through the WISE field of view were included in this analysis, with the exception of a handful of extremely close-approaching NEOs with larger uncertainties that were identifiable by color and morphology (the images were slightly trailed). Astrometric uncertainties were taken from the MPC’s ephemeris service. For objects that were stacked, only objects with very low astrometric uncertainty (less than  $\sim 3$  arcsec) were used. Future work will extend to identifying and stacking objects with larger astrometric uncertainties.

The WISE instrument used three beamsplitters to collect images in all four bands simultaneously (3.4, 4.6, 12 and 22  $\mu\text{m}$ , hereafter W1, W2, W3, and W4). The exposure time in all four WISE bands was set to 8.8 sec in bands W3 and W4 and 7.7 sec in bands W1 and W2. An NEO moving faster than  $\sim 17^\circ/\text{day}$  could thus be trailed in the 6.5 arcsec W3 beam. All candidate images were visually inspected for evidence of trailing. If the images were trailed, aperture magnitudes reported by the data reduction pipeline (denoted  $w1\text{mag}_x$ ,  $w2\text{mag}_x$ ,  $w3\text{mag}_x$ , and  $w4\text{mag}_x$ , where 1-4 represents the wavelength band, 1-4, and  $x$  represents the number of the aperture that encircled the source, 1-8) were used instead of photometry derived using point-spread function fits; see Section IV.4.c of the WISE Explanatory Supplement (Cutri et al. 2012) for a detailed description of the WISE pipeline photometry. Aperture curves-of-growth were constructed for the trailed objects, and the aperture at which the curve converged was selected.

For objects that were too faint to be detected reliably in single exposures, the single exposure images were coadded in the moving frame of the asteroid, aligning the frames using each object’s ephemeris, with the ICORE (Image Co-addition with Optional Resolution Enhancement) stacking algorithm (Masci & Fowler 2009; Masci 2013). The ICORE algorithm includes outlier rejection and resamples the stacked image to a pixel scale of 1 arcsec/pixel. The algorithm requires a minimum of five images to ensure adequate pixel outlier rejection; all coadded objects in this analysis exceeded this number of images. An example of an object recovered in the NEOWISE data by stacking with ICORE is shown in Figure 1, demonstrating the utility of this technique for obtaining infrared detections of minor planets that fell just below the single frame detection threshold; similar success with the extended object comet 17P/Holmes was shown in Stevenson et al. (2013). For the stacked objects, aperture photometry was performed using radii of 11, 11, 11, and 22 arcsec, respectively, in the four WISE bands. Table 1 lists the magnitudes and apertures used for each object.

## 2.1. Thermal Modeling and Error Analysis

The Near-Earth Asteroid Thermal Model (NEATM; Harris 1998) was used to determine diameters and albedos for most objects. The color corrections and modifications that account for the observed discrepancy between red and blue calibrators noted in Wright et al. (2010) were applied following the methods described in Mainzer et al. (2011c). Table 2 shows the thermal fit results for the 106 NEOs that were recovered here; Figure 2 shows an example of a small ( $\sim 8$  m) NEO identified in the NEOWISE data using the IRSA/WISE Image Service and KSSOPAL.

As described in Mainzer et al. (2011a) and Mainzer et al. (2011c), the so-called beaming parameter  $\eta$  employed by the NEATM was fit when two or more thermally-dominated infrared bands were available. Since an NEO’s flux at 3.4 and 4.6  $\mu\text{m}$  generally consists of a mix of thermal emission and reflected sunlight, it was necessary to fit for the reflectivity at these wavelengths. Albedo was assumed to be the same for both 3.4 and 4.6  $\mu\text{m}$ . This simplifying assumption may not always be valid. Grav et al. (2012a) and Grav et al. (2012b) have shown that albedo varies between 3.4 and 4.6  $\mu\text{m}$  for Hilda group asteroids and Jovian Trojans, although the NEOs’ smaller heliocentric distances and warmer temperatures means that the 4.6  $\mu\text{m}$  band is often thermally-dominated, lessening the effect of albedo at 4.6  $\mu\text{m}$  on the total flux. The infrared flux,  $p_{IR} = p_{3.4\mu\text{m}} = p_{4.6\mu\text{m}}$ , could only be fit when the flux at 3.4  $\mu\text{m}$  was dominated by reflected sunlight, which depends on both reflectivity and heliocentric distance.

The best-fit values for diameter, visible geometric albedo  $p_V$ , infrared albedo  $p_{IR}$ , and beaming parameter  $\eta$  were determined using a least-squares optimization that accounted for the measurement uncertainties for bands W1, W2, W3, W4, absolute magnitude  $H$ , and phase curve slope parameter  $G$ .  $G$  was generally taken to be  $0.15 \pm 0.1$  unless a measurement was available (Bowell et al. 1989). Errors on  $H$  ( $\sigma_H$ ) were assumed to be 0.3 mag, although in some cases, examination of the MPC observations file revealed the uncertainty in  $H$  to be considerably larger; in these cases,  $H$  was assumed to be unknown and was not used in the thermal fit. Poorly known  $H$  and  $G$  values continue to be a persistent difficulty that sometimes inhibits precise determination of albedo, although this problem does not much affect the determination of diameter when using radiometric methods such as NEATM.

Although there is evidence that systematic biases in  $H$  magnitudes may be present in the existing asteroid databases such as MPC and *Horizons* that derive  $H$  using measurements made primarily for improvements to astrometry rather than accurate photometry, targeted measurements of  $H$  (e.g. Pravec et al. 2012) have concentrated on objects with  $H \leq 21$  mag. We therefore chose not to adopt a blanket offset to all  $H$  values and instead bounded the errors by assuming  $\sigma_H = 0.3$  mag. The errors in diameter,  $p_V$ ,  $p_{IR}$ , and  $\eta$  were determined

through the use of Monte Carlo trials that varied the measured values of  $W1$ ,  $W2$ ,  $W3$ ,  $W4$ ,  $H$ , and  $G$  by their respective errors. If  $p_{IR}/p_V$  could not be fit, the default value was taken to be the average value determined in Mainzer et al. (2011a) for NEOs, or  $1.6 \pm 1.0$ .

Another source of error is that the slope parameter  $G$  is known to vary with taxonomic type; C-complex asteroids typically have lower  $G$  values, closer to 0.05-0.10, whereas S-complex asteroids have  $G$  closer to 0.2, and the highest albedo classes such as E-types have  $G \sim 0.4$  (Harris et al. 1989; Harris & Young 1989; Lagerkvist & Magnusson 1990; Oszkiewicz et al. 2012). Our generic assumption of  $G = 0.15$  can therefore yield  $H$  values that are too high for C-type objects, which in turn result in overly low values of  $p_V$ . Similarly, our assumed  $G$  value of 0.15 is likely to be too low for S-complex objects, particularly E- and V-types, resulting in  $H$  values that are erroneously low. These effects will be more pronounced at the high phase angles at which NEOWISE typically observed small NEOs and Hungarias. Erroneous values of  $G$  and  $H$  do not much affect diameters derived from thermal measurements, but rather albedo. For example, assuming that 2010 TN<sub>4</sub> has  $G = 0.05$  instead of  $G = 0.15$  results in an offset to  $H$  of -0.28 mag at its NEOWISE-observed phase angle of 80.6°. The derived diameter (18 m) is unchanged, but  $p_V=0.071$  instead of 0.054.

However, without knowledge of an object’s spectral type, we cannot know for certain which value of  $G$  to choose if it has not been directly measured. In our previous works (e.g. Mainzer et al. 2011d, 2012a), we found that there is not a perfect correlation between albedo and taxonomic type. We therefore chose not to apply offsets to  $G$  based on assumed spectral type (which in most cases we could only assume based on albedo - a circular argument). Instead, we model and bound the errors caused by imperfect knowledge of  $G$  by assuming that  $G$  varies by  $\pm 0.10$  in the Monte Carlo trial fits for each object. It is important to note that errors in  $G$  and  $H$  could cause systematic offsets in albedo, with lower albedo objects’ albedos sometimes being too low, and higher albedo objects’ albedos coming out too high. For this reason, direct measurements of  $H$ ,  $G$ , and spectral type for individual objects would be useful, particularly when determining albedos of objects observed at high phase angles. Nevertheless, a major benefit of radiometric fits to infrared observations is that while errors in  $H$  and  $G$  can affect albedo, they cause little change to diameter.

## 2.2. Results

Figure 3 shows the beaming distribution for the small, close-approaching NEOs recovered from the NEOWISE data compared with the sample of 429 NEOs detected by WMOPS during the fully cryogenic portion of the mission. The close-approaching NEOs tend to have been observed near 90° phase, because the WISE spacecraft only observed near 90° solar

elongation (Wright et al. 2010). Thus, the objects were typically observed near their local terminators. The NEATM assumes zero flux contribution from the night side of the asteroids. Because small NEOs are frequently rapidly rotating with rotation periods much less than the cooling timescale (Pravec et al. 2008; Hergenrother & Whiteley 2011; Statler et al. 2013), the approximation of zero night side flux is likely inappropriate in many cases. Indeed, the beaming parameter  $\eta$ , which is used by the NEATM to compensate for the “beaming” effect of radiation observed near zero phase angle, converges to its theoretical maximum value of  $\pi$  in many cases when more than one thermally dominated band is available. The average value found for the small NEOs reported in this work was  $2.0 \pm 0.5$ , higher than the  $1.4 \pm 0.5$  reported for all NEOs over a wide range of phase angles in Mainzer et al. (2011b). Therefore, if  $\eta$  could not be fit, a default value of  $2.0 \pm 0.5$  was used for objects observed close to  $90^\circ$  phase angle. However, we note that while a fit yielding the theoretical maximum value of  $\eta = \pi$  may indeed indicate high thermal inertia and/or rapid rotation, it could also be that the NEATM’s assumption of zero nightside flux is inappropriate for asteroids observed at very high phase angles. At high phase angles, a substantial portion of the nightside hemisphere is visible, so the approximation of zero nightside flux contribution may be poor. Furthermore, for the very smallest objects, the heat conduction length scale begins to approach the object size.

In cases where  $\eta = \pi$  resulted from the NEATM fit, the Fast Rotating Model (FRM; Lebofsky et al. 1978; Lebofsky & Spencer 1989; Veeder et al. 1978) was used instead. In the FRM, the asteroid is assumed to be rotating rapidly compared to its cooling timescale, so that the temperature is isotropic with respect to longitude and varies only with local latitude, assuming that the object’s rotational axis is perpendicular to the Earth-Sun line. The FRM uses fast rotation to smooth out longitudinal temperature variations, although it still has latitudinal temperature variations. The timescale for these to change is seasonal, so thermal conduction (especially in a solid boulder) could lead to uniform temperature in longitude. When using the FRM, we made the assumption that the rotational pole is perpendicular to the plane defined by the Sun, Earth, and object. This assumption may be reasonable given that there is evidence that the non-gravitational thermal pressure torques exerted by the YORP effect are thought to drive small asteroids to this state. For objects in the 10 - 100 m size range, the mean time between spin axis reorientation due to collisions is thought to be much longer than the timescale over which YORP will reshape spin states (Farinella et al. 1998; Rossi et al. 2009). Using the FRM instead of the NEATM usually has the effect of shrinking an object’s best-fit effective spherical diameter, since the flux that was distributed across only one hemisphere using the NEATM is now spread across the entire visible area; diameter must therefore shrink to conserve the emitted energy.

With so few observations (in some cases only one), the rotational lightcurves of many

NEOs in this sample were not well-sampled. For the WMOPS-detected sample, the WISE observational cadence typically resulted in 10-12 observations of each object collected over a  $\sim 36$  hour span. The question is the extent to which diameters determined using only sparse detections are representative of the actual effective spherical diameter. As shown in figure 5 in Mainzer et al. (2011a), most NEOs detected by NEOWISE had lightcurve amplitudes of  $\sim 0.4$  mag or less.

Two effects come into play when one attempts to use sparse detections near the sensitivity limit to investigate a population. First, there is a systematic bias in flux measurements that are made very close to the noise limit of a detector. Random noise can scatter flux above the detection threshold, making a source appear brighter. This manifestation of the Eddington bias was observed with WISE’s predecessor, the *Infrared Astronomical Satellite*<sup>2</sup>. Second, asteroids rotate, and they can be elongated. The tendency would be to detect a rotating, elongated body when it is closer to presenting its maximum surface area to the observer. Both of these effects combine to produce an overestimate of fluxes for small bodies observed by WISE only a handful of times.

In an effort to better understand the effects of sparsely sampled infrared lightcurves on thermal model outputs, a comparison was made between fits using the entire set of NEOWISE thermal measurements for each object and fits derived using only the single brightest point per object. Because WISE observes in all four bands simultaneously using beamsplitters, we selected the time at the maximum of the lightcurve in the band with the highest signal-to-noise ratio, then used all bands available at that time. Figure 4 (top) shows  $\Delta D = (D_{all} - D_{max})/D_{all}$ , where  $D_{all}$  is the diameter derived using all points, and  $D_{max}$  are the diameters resulting from the maximum brightnesses, as a function of  $D_{all}$ . Over most size ranges, the dispersion between  $D_{max}$  and  $D_{all}$  is typically a factor of  $\sim 1.3$ , although it worsens at smaller sizes. In most cases, the tendency is unsurprisingly to overestimate the diameter when using only the observations at the maximum of a lightcurve. However, at smaller sizes in particular,  $D_{max}$  can be observed in Figure 4 to be approximately double  $D_{all}$ .

Unfortunately, this analysis cannot account for the possibility of real variations in the shapes of NEOs at sizes smaller than the WMOPS-selected sample shown in Figure 4. Very small NEOs might have shapes that are either more round or more irregular than larger objects, depending on their origins and subsequent evolution. The observed amplitude of an asteroid’s light curve depends on the interplay between the shape of the object, the orientation of the rotation pole with respect to the line of sight, and the phase angle of the

---

<sup>2</sup><http://irsa.ipac.caltech.edu/IRASdocs/exp.sup/ch11/J.html>



object at the time of observation when using reflected light. To first order, the larger the axial ratios of the object, the larger the amplitude of the light curve will be. However, if the sub-observer point is near the rotation pole, the light curve amplitude will be reduced.

Amplitudes larger than two magnitudes have been seen at optical wavelengths for small NEOs that are a result of very elongated shapes (e.g. 2009 UU<sub>1</sub>; Warner et al. 2009). However, small amplitudes are frequently observed by WISE, implying either a shape close to spherical or an observing geometry looking along the rotation pole. Nevertheless, the analysis described above suggests that the sizes derived from sparse observations can serve as valuable upper limits to NEO sizes, and it is therefore quite likely that many of the objects presented in Table 2 are somewhat smaller than their derived sizes. The error bars reported in Table 2 are the formal errors resulting from the Monte Carlo trials that vary the WISE magnitudes,  $H$ , and  $G$  by their respective error bars, and they do not include the systematic errors that may be associated with the sparseness of some of the lightcurve sampling. A typical systematic error for the sizes given in Table 2 is likely to be of order the  $\sim 30\%$  shown in Figure 4, although in some cases, it is possible that the derived sizes are quite different.

The structure of asteroids smaller than 100 m is uncertain. Pravec et al. (2008) have shown that while asteroids larger than a few hundred meters show a spin limit coincident with the theoretical maximum rotation rate of a gravitationally bound rubble pile, smaller asteroids typically rotate well above this limit, which was interpreted as evidence that these objects were monolithic. Scheeres et al. (2010) showed that cohesive forces on small grains ( $< 1$  cm) can be sufficient to allow small rubble piles to rotate at rates above the spin barrier without disrupting. However, in the process of forming these objects, any monolithic components of the original body could be ejected onto independent orbits, becoming NEOs in their own right. Thus, there may be different kinds of small NEOs. Monolithic fragments created by the breakup of larger bodies will have shape distributions determined by the impact and fracture processes of the collisions that generated them, which may vary among collisions. Objects held together by cohesive forces may have a range of shapes allowed by the force balance, from nearly spherical to oblong. While it is beyond the scope of this work to constrain these shape distributions and the division between monolithic and cohesive objects, we can regard the diameters derived from sparsely sampled lightcurves as, at worst, useful upper limits.

*2009 BD.* One of the objects shown in Table 2, 2009 BD, passed through the WISE fields of view but was not detected even when the images were stacked. However, it is possible to use the images to set an upper limit on its size from the non-detection. We extracted magnitudes from 13 images coadded using ICORE, taken on June 13 and 14 of 2010 (during the fully cryogenic mission phase) at a phase angle of  $88^\circ$ , using aperture photometry with a

sample radius of 11 arcsec. The counts yielded a  $5 - \sigma$  magnitude limit of 11.77 for W3, our most sensitive band for NEOs, and 7.59 mag for W4. Given that 2009 BD was discovered by a visible light telescope (the Catalina Sky Survey), Figure 5 suggests that it is more likely to have a higher albedo than a lower albedo. Using the NEATM fit code, this magnitude limit corresponds to a  $5 - \sigma$  effective spherical diameter upper limit of  $\sim 14.5$  m, assuming  $p_V=0.2$  and  $\eta=2.0$ ; using  $p_V=0.04$  produces an upper limit of 14 m. The FRM results in a  $5 - \sigma$  upper limit of 8 m.

### 2.3. Discussion

Figure 5 shows the diameters and albedos of the optically-selected sample of small NEOs recovered from the NEOWISE data compared with the infrared-selected sample drawn using WMOPS from Mainzer et al. (2011a). All recoveries were discovered by visible light telescopes, which are preferentially biased against discovering small, dark NEOs. The infrared-selected sample’s albedo distribution is essentially flat with diameter, whereas the optically-selected sample’s albedos increase with decreasing diameter. While there may be real physical changes in albedo with diameter, the visible light survey biases against discovering small, dark NEOs complicate efforts to determine the true albedo distribution of the population of small NEOs. It is also apparent that the current suite of visible light survey telescopes is not efficient at discovering very tiny low albedo NEOs.

While one might be tempted to use the albedo distribution for tiny NEOs shown in Figure 5 to extrapolate to the total number of NEOs in the population (c.f. Mainzer et al. 2011a, 2012c), we caution that this is not an infrared-selected sample with well-determined survey biases. All objects presented here were discovered by ground-based visible light surveys that are subject to the effects of weather and seeing variations, in addition to the NEOWISE detection biases. Debiasing this sample requires careful modeling of all of these selection effects, and for objects in this size range, infrasound measurements of small meteors and cratering studies should be included (c.f. the lunar impact flash studies such as Oberst et al. 2012; Suggs et al. 2008) to provide a realistic assessment of their true numbers, sizes, and albedos.

## 3. Conclusions

We have reported sizes, albedos, and thermal model parameters such as beaming for 106 NEOs, roughly half of which are smaller than 100 m in effective spherical diameter, and

the smallest of which are  $\sim 8$  m. These objects generally were not detected by the automated WMOPS survey because they were too faint in the individual images or were not detected the required five times for the pipeline to trigger on them. Many of the objects were extremely close to Earth when they were observed by WISE, with  $\sim 10$  m NEOs being detectable only when they approached within several lunar distances. Because close NEOs tend to move with large apparent velocities, many of the objects were only detected a handful of times; approximately one-third of the sample reported here was detected only once. While radiometric thermal models are typically able to constrain the sizes of asteroids when lightcurves are well-sampled, the results of models using these sparsely-sampled lightcurves must be regarded with caution. We have attempted to estimate the degree to which thermal models of NEOs using sparse data will err in their predictions of effective spherical diameter. We find that in most cases, typical errors are  $\sim 30\%$  if one assumes that the distribution of shapes for NEOs smaller than  $\sim 100$  m is similar to those larger than 100 m. However, in some cases, the size is overestimated by factors of several. Nonetheless, sparse infrared data can still provide useful estimates of effective spherical diameters.

We have shown that our sample of small NEOs displays a marked trend of increasing albedo with decreasing diameter, but given that the optical surveys that discovered this sample are biased against finding small, dark, faint NEOs, this is not surprising. These data alone are insufficient to determine whether or not this result represents a real physical trend or merely selection effects, as the optical surveys are highly incomplete at these small sizes. Selection biases must be carefully disentangled using models of survey performance. It is, however, clear that much work remains to be done to discover and characterize the population of very small NEOs.

#### 4. Acknowledgments

This publication makes use of data products from the *Wide-field Infrared Survey Explorer*, which is a joint project of the University of California, Los Angeles, and the Jet Propulsion Laboratory/California Institute of Technology, funded by the National Aeronautics and Space Administration. This publication also makes use of data products from NEOWISE, which is a project of the Jet Propulsion Laboratory/California Institute of Technology, funded by the Planetary Science Division of the National Aeronautics and Space Administration. We thank our referee, Dr. Alan Harris of Pasadena, for his helpful comments that materially improved this manuscript. We gratefully acknowledge the extraordinary services specific to NEOWISE contributed by the International Astronomical Union’s Minor Planet Center, operated by the Harvard-Smithsonian Center for Astrophysics, and the Cen-

tral Bureau for Astronomical Telegrams, operated by Harvard University. We also thank the worldwide community of dedicated amateur and professional astronomers devoted to minor planet follow-up observations. This research has made use of the NASA/IPAC Infrared Science Archive, which is operated by the California Institute of Technology, under contract with the National Aeronautics and Space Administration.

## REFERENCES

- Bottke, W. F., Morbidelli, A., Jedicke, R., Petit, J.-M., Levison, H. F., Michel, P., & Metcalfe, T. S. 2002, *Icarus*, 156, 399
- Bowell, E., Hapke, B., Domingue, D., Lumme, K., Peltoniemi, J., & Harris, A. W. 1989, in *Asteroids II*, ed. R. P. Binzel, T. Gehrels, & M. S. Matthews, 524–556
- Cutri, R. M., Wright, E. L., Conrow, T., Bauer, J., Benford, D., Brandenburg, H., Dailey, J., Eisenhardt, P. R. M., Evans, T., Fajardo-Acosta, S., Fowler, J., Gelino, C., Grillmair, C., Harbut, M., Hoffman, D., Jarrett, T., Kirkpatrick, J. D., Leisawitz, D., Liu, W., Mainzer, A., Marsh, K., Masci, F., McCallon, H., Padgett, D., Ressler, M. E., Royer, D., Skrutskie, M. F., Stanford, S. A., Wyatt, P. L., Tholen, D., Tsai, C. W., Wachter, S., Wheelock, S. L., Yan, L., Alles, R., Beck, R., Grav, T., Masiero, J., McCollum, B., McGehee, P., Papin, M., & Wittman, M. 2012, 1
- Farinella, P., Vokrouhlicky, D., & Hartmann, W. K. 1998, *Icarus*, 132, 378
- Fowler, J. W. & Chillemi, J. R. 1992, *The IRAS Minor Planet Survey*, Phillips Laboratory, Hanscom AF Base, MA, Tech. Rep. PL-TR-92-2049, 17
- Grav, T., Mainzer, A. K., Bauer, J., Masiero, J., Spahr, T., McMillan, R. S., Walker, R., Cutri, R., Wright, E., Eisenhardt, P. R., Blauvelt, E., DeBaun, E., Elsbury, D., Gautier, T., Gomillion, S., Hand, E., & Wilkins, A. 2012a, *ApJ*, 744, 197
- Grav, T., Mainzer, A. K., Bauer, J., Masiero, J., Spahr, T., McMillan, R. S., Walker, R., Cutri, R., Wright, E., Eisenhardt, P. R. M., Blauvelt, E., DeBaun, E., Elsbury, D., Gautier, IV, T., Gomillion, S., Hand, E., & Wilkins, A. 2011, *ApJ*, 742, 40
- Grav, T., Mainzer, A. K., Bauer, J. M., Masiero, J. R., & Nugent, C. R. 2012b, *ApJ*, 759, 49
- Harris, A. 2008, *Nature*, 453, 1178
- Harris, A. W. 1998, *Icarus*, 131, 291
- Harris, A. W. & Young, J. W. 1989, *Icarus*, 81, 314
- Harris, A. W., Young, J. W., Contreiras, L., Dockweiler, T., Belkora, L., Salo, H., Harris, W. D., Bowell, E., Poutanen, M., Binzel, R. P., Tholen, D. J., & Wang, S. 1989, *Icarus*, 81, 365
- Hergenrother, C. W. & Whiteley, R. J. 2011, *Icarus*, 214, 194

- Jedicke, R. & Metcalfe, T. S. 1998, *Icarus*, 131, 245
- Lagerkvist, C.-I. & Magnusson, P. 1990, *A&AS*, 86, 119
- Lebofsky, L. A. & Spencer, J. R. 1989, in *Asteroids II*, ed. R. P. Binzel, T. Gehrels, & M. S. Matthews, 128–147
- Lebofsky, L. A., Veeder, G. J., Lebofsky, M. J., & Matson, D. L. 1978, *Icarus*, 35, 336
- Mainzer, A., Bauer, J., Grav, T., Masiero, J., Cutri, R. M., Dailey, J., Eisenhardt, P., McMillan, R. S., Wright, E., Walker, R., Jedicke, R., Spahr, T., Tholen, D., Alles, R., Beck, R., Brandenburg, H., Conrow, T., Evans, T., Fowler, J., Jarrett, T., Marsh, K., Masci, F., McCallon, H., Wheelock, S., Wittman, M., Wyatt, P., DeBaun, E., Elliott, G., Elsbury, D., Gautier, IV, T., Gomillion, S., Leisawitz, D., Maleszewski, C., Micheli, M., & Wilkins, A. 2011a, *ApJ*, 731, 53
- Mainzer, A., Grav, T., Bauer, J., Masiero, J., McMillan, R. S., Cutri, R. M., Walker, R., Wright, E., Eisenhardt, P., Tholen, D. J., Spahr, T., Jedicke, R., Denneau, L., DeBaun, E., Elsbury, D., Gautier, T., Gomillion, S., Hand, E., Mo, W., Watkins, J., Wilkins, A., Bryngelson, G. L., Del Pino Molina, A., Desai, S., Gómez Camus, M., Hidalgo, S. L., Konstantopoulos, I., Larsen, J. A., Maleszewski, C., Malkan, M. A., Mauduit, J.-C., Mullan, B. L., Olszewski, E. W., Pforr, J., Saro, A., Scotti, J. V., & Wasserman, L. H. 2011b, *ApJ*, 743, 156
- Mainzer, A., Grav, T., Masiero, J., Bauer, J., Cutri, R. M., McMillan, R. S., Nugent, C. R., Tholen, D., Walker, R., & Wright, E. L. 2012a, *ApJ*, 760, L12
- Mainzer, A., Grav, T., Masiero, J., Bauer, J., McMillan, R. S., Giorgini, J., Spahr, T., Cutri, R. M., Tholen, D. J., Jedicke, R., Walker, R., Wright, E., & Nugent, C. R. 2012b, *ApJ*, 752, 110
- Mainzer, A., Grav, T., Masiero, J., Bauer, J., Wright, E., Cutri, R. M., McMillan, R. S., Cohen, M., Ressler, M., & Eisenhardt, P. 2011c, *ApJ*, 736, 100
- Mainzer, A., Grav, T., Masiero, J., Bauer, J., Wright, E., Cutri, R. M., Walker, R., & McMillan, R. S. 2011d, *ApJ*, 737, L9
- Mainzer, A., Masiero, J., Grav, T., Bauer, J., Tholen, D. J., McMillan, R. S., Wright, E., Spahr, T., Cutri, R. M., Walker, R., Mo, W., Watkins, J., Hand, E., & Maleszewski, C. 2012c, *ApJ*, 745, 7
- Masci, F. 2013, ICORE: Image Co-addition with Optional Resolution Enhancement, *astrophysics Source Code Library*

- Masci, F. J. & Fowler, J. W. 2009, in *Astronomical Society of the Pacific Conference Series*, Vol. 411, *Astronomical Data Analysis Software and Systems XVIII*, ed. D. A. Bohlender, D. Durand, & P. Dowler, 67
- Oberst, J., Christou, A., Suggs, R., Moser, D., Daubar, I. J., McEwen, A. S., Burchell, M., Kawamura, T., Hiesinger, H., Wünnemann, K., Wagner, R., & Robinson, M. S. 2012, *Planet. Space Sci.*, 74, 179
- Oszkiewicz, D. A., Bowell, E., Wasserman, L. H., Muinonen, K., Penttilä, A., Pieniluoma, T., Trilling, D. E., & Thomas, C. A. 2012, *Icarus*, 219, 283
- Pravec, P., Harris, A. W., Kušnirák, P., Galád, A., & Hornoch, K. 2012, *Icarus*, 221, 365
- Pravec, P., Harris, A. W., Vokrouhlický, D., Warner, B. D., Kušnirák, P., Hornoch, K., Pray, D. P., Higgins, D., Oey, J., Galád, A., Gajdoš, Š., Kornoš, L., Világi, J., Husárik, M., Krugly, Y. N., Shevchenko, V., Chiorny, V., Gaftonyuk, N., Cooney, W. R., Gross, J., Terrell, D., Stephens, R. D., Dyvig, R., Reddy, V., Ries, J. G., Colas, F., Lecacheux, J., Durkee, R., Masi, G., Koff, R. A., & Goncalves, R. 2008, *Icarus*, 197, 497
- Rossi, A., Marzari, F., & Scheeres, D. J. 2009, *Icarus*, 202, 95
- Scheeres, D. J., Hartzell, C. M., Sánchez, P., & Swift, M. 2010, *Icarus*, 210, 968
- Spahr, T. B. 1998, PhD thesis, University of Florida
- Statler, T. S., Cotto-Figueroa, D., Riethmiller, D. A., & Sweeney, K. M. 2013, *Icarus*, 225, 141
- Stevenson, R., Bauer, J., Kramer, E., Grav, T., Mainzer, A., & Masiero, J. 2013, *ApJ*, submitted
- Stuart, J. S. & Binzel, R. P. 2004, *Icarus*, 170, 295
- Suggs, R. M., Cooke, W. J., Suggs, R. J., Swift, W. R., & Hollon, N. 2008, *Earth Moon and Planets*, 102, 293
- Trilling, D. E., Mueller, M., Hora, J. L., Harris, A. W., Bhattacharya, B., Bottke, W. F., Chesley, S., Delbo, M., Emery, J. P., Fazio, G., Mainzer, A., Penprase, B., Smith, H. A., Spahr, T. B., Stansberry, J. A., & Thomas, C. A. 2010, *AJ*, 140, 770
- Veeder, G. J., Matson, D. L., & Smith, J. C. 1978, *AJ*, 83, 651
- Warner, B. D., Harris, A. W., & Pravec, P. 2009, *Icarus*, 202, 134

Wright, E. L., Eisenhardt, P. R. M., Mainzer, A. K., Ressler, M. E., Cutri, R. M., Jarrett, T., Kirkpatrick, J. D., Padgett, D., McMillan, R. S., Skrutskie, M., Stanford, S. A., Cohen, M., Walker, R. G., Mather, J. C., Leisawitz, D., Gautier, III, T. N., McLean, I., Benford, D., Lonsdale, C. J., Blain, A., Mendez, B., Irace, W. R., Duval, V., Liu, F., Royer, D., Heinrichsen, I., Howard, J., Shannon, M., Kendall, M., Walsh, A. L., Larsen, M., Cardon, J. G., Schick, S., Schwalm, M., Abid, M., Fabinsky, B., Naes, L., & Tsai, C.-W. 2010, *AJ*, 140, 1868



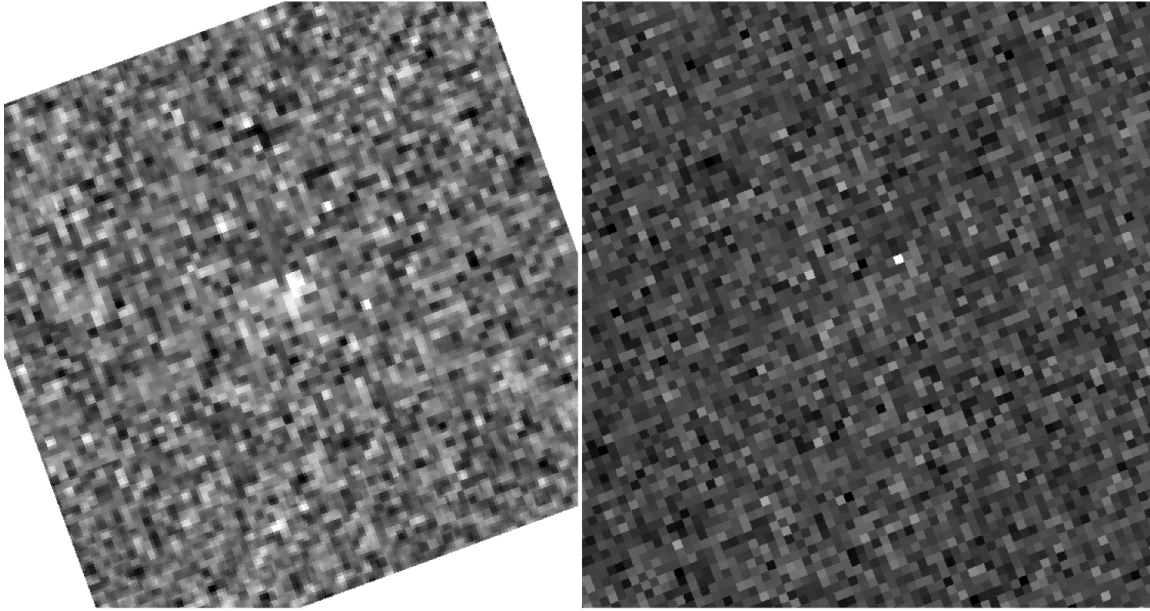


Fig. 1.— Left: The NEO 2010 FK (center of image) was only detected in W3 by creating a moving coadd that combined 13 exposures, as it fell just below the detection threshold in the single-frame images (right, center of image).

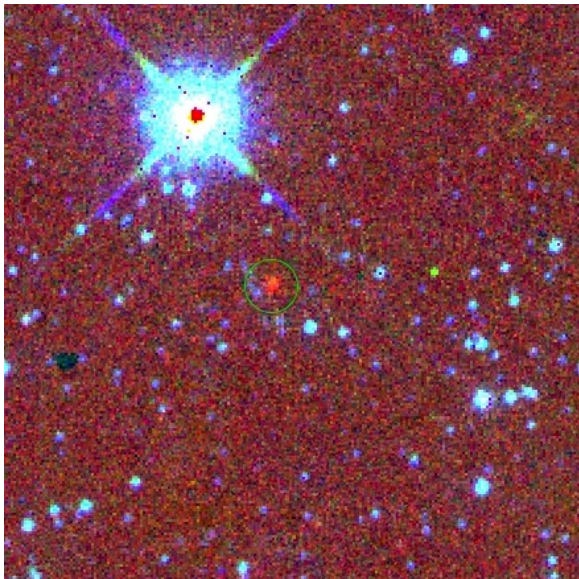


Fig. 2.— The NEO 2010 GH<sub>7</sub> (circled in green) was detected only once by NEOWISE due to its high apparent on-sky velocity in bands W2, W3, and W4. This object is on the list of accessible targets for potential human exploration; it makes close approaches to Earth every  $\sim 5$  years. Blue = band W1; green = W2; red = W3.

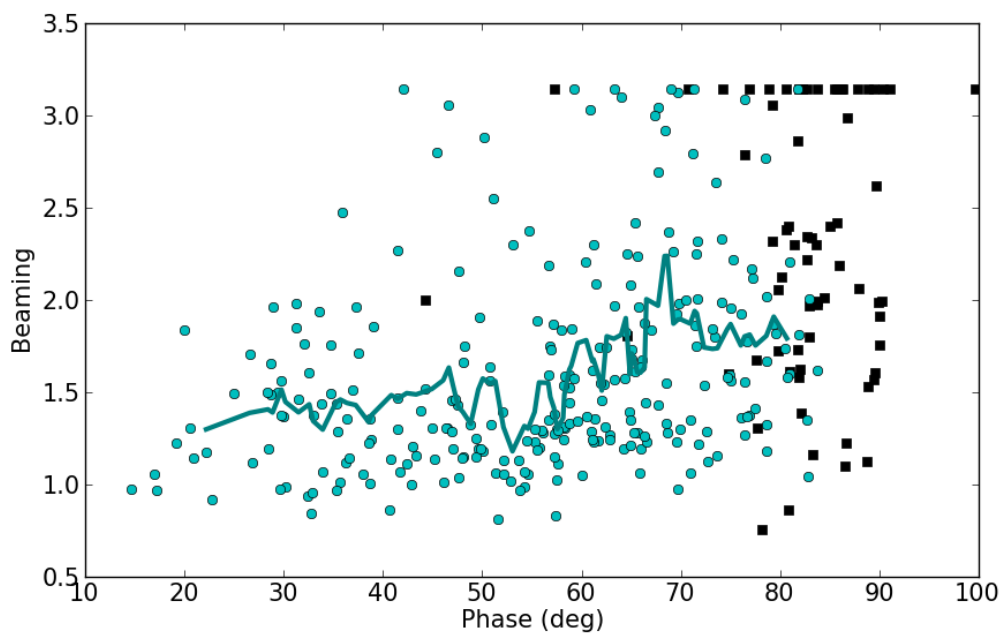


Fig. 3.— Beaming parameter vs. phase angle for objects observed in two or more thermal wavelengths. The small, close-approaching NEOs that were detected by NEOWISE using the KSSOPAL and WISE Image Service tools (black squares) were usually observed at very high phase angles; the beaming parameter  $\eta$  required was significantly larger than the average value for NEOs observed at lower phase angles (cyan points; cyan line shows running median). Cyan points taken from Mainzer et al. (2011a). Only objects with more than one thermally-dominated band available are plotted as these are the objects for which  $\eta$  can be fit; the maximum value of  $\eta = \pi$ .

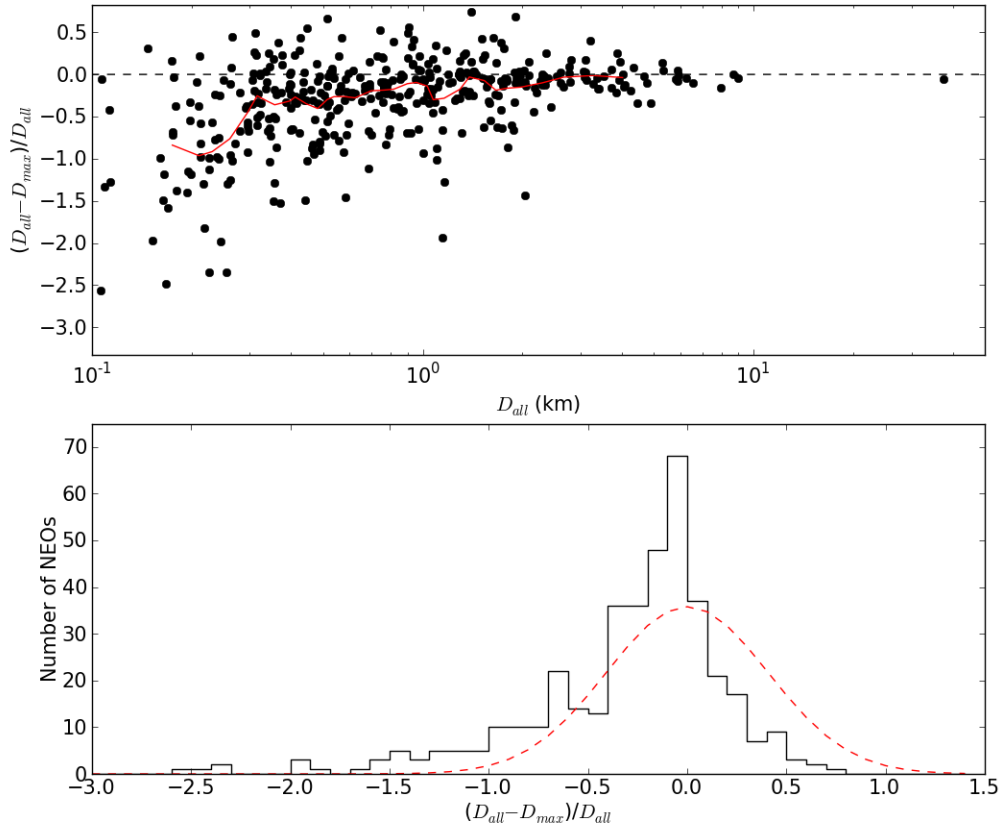


Fig. 4.— Top: Comparison between NEATM diameter fits derived using the full set of NEOWISE measurements for each NEO vs. fits derived using only the brightest measurement in W3 for each object; the red line shows a running median. Bottom: Histogram of diameter differences between full lightcurve fits and maximum brightness fits; a Gaussian is overplotted (red dashed line).

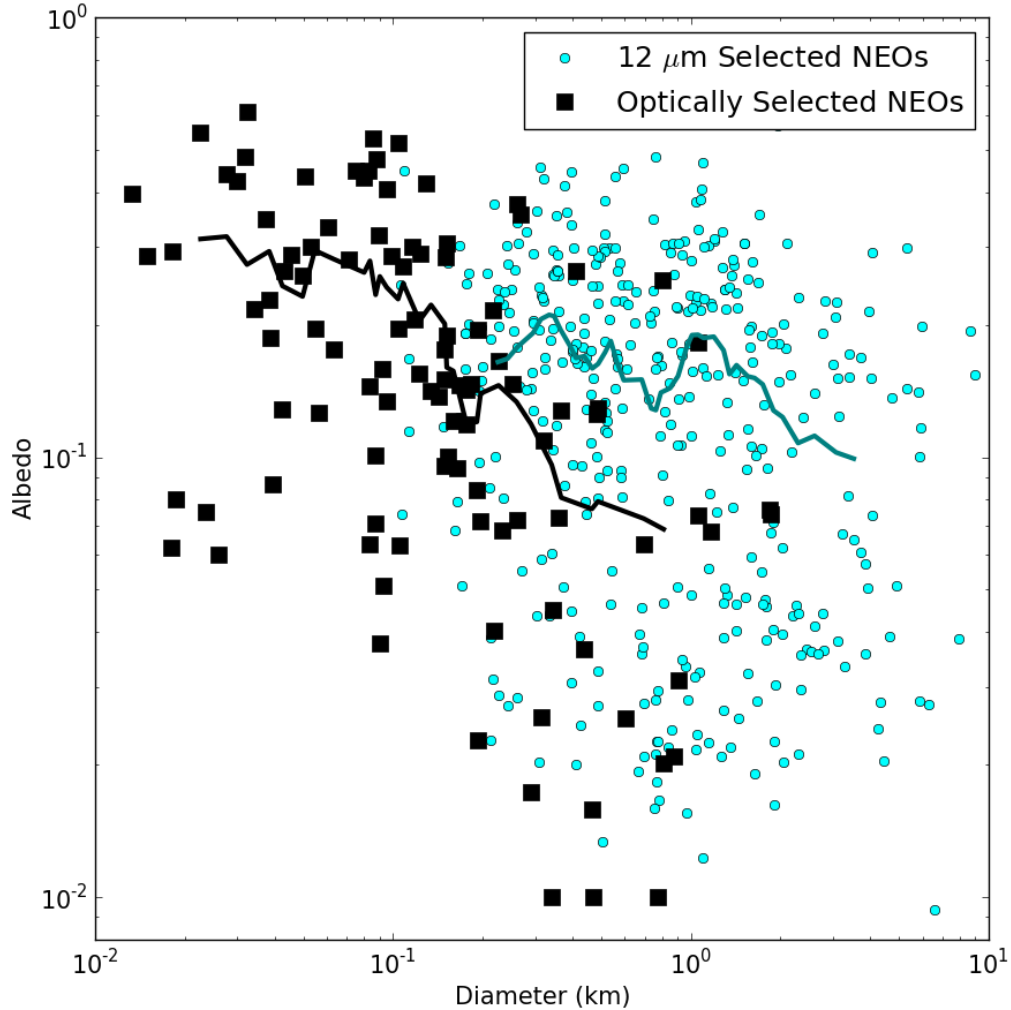


Fig. 5.— The sample of objects recovered from the NEOWISE dataset using the KSSOPAL and WISE Image Service tools were all discovered by visible light ground-based surveys (black squares). The albedo distribution of these objects is distinctly different from the sample of NEOs that were selected using the WMOPS algorithm working on 12  $\mu\text{m}$  NEOWISE data (cyan circles). Because the WMOPS algorithm treated new discoveries the same way as recoveries of previously known objects, and because asteroids’ thermal fluxes depend only weakly on albedo, the 12  $\mu\text{m}$  sample is albedo-insensitive. The optically-selected sample’s albedo distribution increases sharply with decreasing size (black line), whereas the albedo distribution of the infrared-selected sample (cyan line) remains essentially unchanged with decreasing size.

Table 1. Observed WISE magnitudes for each of the NEOs presented here, including the modified Julian date (MJD). Objects that were not detected at a particular wavelength represent  $2 - \sigma$  upper limits (Cutri et al. 2012). A value of “–” indicates that no data were available at that wavelength. The final column gives the aperture radius in arcsec used for aperture photometry; “0” indicates that the pipeline profile fit photometry was used. Objects marked with \* were stacked in order to recover their fluxes; for the objects, the stacked image photometry is reported.

Name	MJD	W1 (mag)	W2 (mag)	W3 (mag)	W4 (mag)	Aperture
85989	55310.732616	>16.882	>15.004	9.264 ± 0.081	7.098 ± 0.260	0
85989	55310.86492	>16.703	14.323 ± 0.175	8.765 ± 0.055	6.734 ± 0.198	0
85989	55310.997225	>16.695	14.525 ± 0.266	8.247 ± 0.035	6.260 ± 0.124	0
85989	55311.129529	16.623 ± 0.431	14.170 ± 0.162	8.195 ± 0.035	5.864 ± 0.106	0
85989	55311.261833	16.237 ± 0.300	14.507 ± 0.212	8.598 ± 0.052	6.514 ± 0.161	0
85989	55311.327922	>16.373	14.234 ± 0.171	8.491 ± 0.044	6.320 ± 0.142	0
85989	55311.394137	>17.032	>15.588	8.842 ± 0.056	7.073 ± 0.294	0
85989	55311.460226	>16.506	13.843 ± 0.126	8.190 ± 0.037	6.145 ± 0.113	0
85989	55311.526442	>16.304	15.161 ± 0.375	9.434 ± 0.094	7.656 ± 0.426	0
85989	55311.59253	>16.498	13.954 ± 0.120	8.425 ± 0.040	6.197 ± 0.114	0
85989	55311.592657	>16.636	14.295 ± 0.168	8.395 ± 0.041	6.429 ± 0.154	0
85989	55311.658746	16.835 ± 0.465	14.376 ± 0.182	8.774 ± 0.051	6.872 ± 0.223	0
85989	55311.724834	16.324 ± 0.288	14.618 ± 0.207	8.643 ± 0.049	6.711 ± 0.173	0
85989	55311.857139	>16.664	14.961 ± 0.291	9.144 ± 0.075	6.715 ± 0.183	0
85989	55311.857266	>17.049	15.356 ± 0.434	9.274 ± 0.082	6.908 ± 0.233	0
85989	55311.989443	16.923 ± 0.479	14.216 ± 0.156	8.871 ± 0.058	6.758 ± 0.185	0
85989	55311.98957	>16.486	14.833 ± 0.286	9.028 ± 0.065	7.277 ± 0.308	0
85989	55312.121747	16.674 ± 0.409	13.984 ± 0.129	8.267 ± 0.035	6.370 ± 0.135	0
85989	55312.254051	15.991 ± 0.233	14.235 ± 0.160	8.105 ± 0.038	6.027 ± 0.099	0
85989	55312.254051	15.991 ± 0.233	14.235 ± 0.160	8.105 ± 0.038	6.027 ± 0.099	0
85989	55322.044695	>16.852	13.933 ± 0.162	8.645 ± 0.047	6.643 ± 0.174	0
85989	55406.690608	12.304 ± 0.026	9.050 ± 0.018	3.689 ± 0.012	1.755 ± 0.017	0
85989	55406.756696	11.754 ± 0.023	8.649 ± 0.016	3.753 ± 0.011	2.008 ± 0.030	0
85989	55406.822912	11.803 ± 0.030	8.484 ± 0.019	3.370 ± 0.014	1.590 ± 0.021	0
85989	55406.889	12.697 ± 0.027	9.565 ± 0.021	4.298 ± 0.010	2.359 ± 0.021	0
85989	55310.732616	>16.882	>15.004	9.264 ± 0.081	7.098 ± 0.260	0
85989	55310.86492	>16.703	14.323 ± 0.175	8.765 ± 0.055	6.734 ± 0.198	0
85989	55310.997225	>16.695	14.525 ± 0.266	8.247 ± 0.035	6.260 ± 0.124	0
85989	55311.129529	16.623 ± 0.431	14.170 ± 0.162	8.195 ± 0.035	5.864 ± 0.106	0
85989	55311.261833	16.237 ± 0.300	14.507 ± 0.212	8.598 ± 0.052	6.514 ± 0.161	0
85989	55311.327922	>16.373	14.234 ± 0.171	8.491 ± 0.044	6.320 ± 0.142	0
85989	55311.394137	>17.032	>15.588	8.842 ± 0.056	7.073 ± 0.294	0
85989	55311.460226	>16.506	13.843 ± 0.126	8.190 ± 0.037	6.145 ± 0.113	0
85989	55311.526442	>16.304	15.161 ± 0.375	9.434 ± 0.094	7.656 ± 0.426	0
85989	55311.59253	>16.498	13.954 ± 0.120	8.425 ± 0.040	6.197 ± 0.114	0
85989	55311.592657	>16.636	14.295 ± 0.168	8.395 ± 0.041	6.429 ± 0.154	0
85989	55311.658746	16.835 ± 0.465	14.376 ± 0.182	8.774 ± 0.051	6.872 ± 0.223	0
85989	55311.724834	16.324 ± 0.288	14.618 ± 0.207	8.643 ± 0.049	6.711 ± 0.173	0
85989	55311.857139	>16.664	14.961 ± 0.291	9.144 ± 0.075	6.715 ± 0.183	0
85989	55311.857266	>17.049	15.356 ± 0.434	9.274 ± 0.082	6.908 ± 0.233	0
85989	55311.989443	16.923 ± 0.479	14.216 ± 0.156	8.871 ± 0.058	6.758 ± 0.185	0
85989	55311.98957	>16.486	14.833 ± 0.286	9.028 ± 0.065	7.277 ± 0.308	0
85989	55312.121747	16.674 ± 0.409	13.984 ± 0.129	8.267 ± 0.035	6.370 ± 0.135	0
85989	55312.254051	15.991 ± 0.233	14.235 ± 0.160	8.105 ± 0.038	6.027 ± 0.099	0
85989	55312.254051	15.991 ± 0.233	14.235 ± 0.160	8.105 ± 0.038	6.027 ± 0.099	0
85989	55322.044695	>16.852	13.933 ± 0.162	8.645 ± 0.047	6.643 ± 0.174	0
85989	55406.690608	12.304 ± 0.026	9.050 ± 0.018	3.689 ± 0.012	1.755 ± 0.017	0
85989	55406.756696	11.754 ± 0.023	8.649 ± 0.016	3.753 ± 0.011	2.008 ± 0.030	0
85989	55406.822912	11.803 ± 0.030	8.484 ± 0.019	3.370 ± 0.014	1.590 ± 0.021	0
85989	55406.889	12.697 ± 0.027	9.565 ± 0.021	4.298 ± 0.010	2.359 ± 0.021	0
88254	55272.46093	12.569 ± 0.031	9.723 ± 0.025	4.990 ± 0.011	3.197 ± 0.026	0
88254	55272.527146	12.450 ± 0.025	9.715 ± 0.020	4.971 ± 0.010	3.223 ± 0.026	0
D7032	55473.298128	11.269 ± 0.027	8.454 ± 0.020	–	–	0
D7032	55473.298256	11.372 ± 0.029	8.334 ± 0.019	–	–	0
D7032	55473.364344	11.359 ± 0.025	8.296 ± 0.021	–	–	0
F2742	55225.802684	14.567 ± 0.070	11.976 ± 0.032	6.167 ± 0.014	4.092 ± 0.037	0
F2742	55225.868773	15.267 ± 0.118	12.286 ± 0.040	6.317 ± 0.015	4.134 ± 0.036	0
F2742	55225.8689	15.185 ± 0.117	12.346 ± 0.038	6.249 ± 0.014	4.179 ± 0.040	0
F4590	55373.377953	16.816 ± 0.435	14.859 ± 0.264	8.848 ± 0.061	6.480 ± 0.153	0
F4590	55373.444041	16.723 ± 0.457	>14.936	8.869 ± 0.059	6.789 ± 0.209	0
M6554	55203.412309	15.326 ± 0.127	12.919 ± 0.057	7.121 ± 0.020	5.047 ± 0.053	0
M6554	55203.80926	15.295 ± 0.120	13.179 ± 0.090	7.213 ± 0.021	5.091 ± 0.047	0
M6554	55203.875476	15.556 ± 0.188	13.170 ± 0.069	7.330 ± 0.021	5.239 ± 0.067	0
M6554	55204.073869	15.400 ± 0.140	13.045 ± 0.064	7.074 ± 0.022	5.040 ± 0.045	0
M6554	55386.281957	>12.860	>14.954	>10.718	>7.573	0
M6554	55386.41426	>17.115	>15.676	10.731 ± 0.304	7.157 ± 0.304	0
M6554	55386.546564	>17.023	>15.444	10.518 ± 0.260	>7.863	0

Table 1—Continued

Name	MJD	W1 (mag)	W2 (mag)	W3 (mag)	W4 (mag)	Aperture
M6554	55386.678868	>16.901	>15.096	10.410 ± 0.239	>7.129	0
M6554	55386.811171	>16.550	14.962 ± 0.318	10.662 ± 0.293	>7.407	0
M6554	55386.877387	16.712 ± 0.419	>15.551	>10.911	7.257 ± 0.308	0
M6554	55387.009691	>16.977	>14.912	10.847 ± 0.347	7.713 ± 0.469	0
M6554	55387.141994	16.700 ± 0.407	15.178 ± 0.382	10.995 ± 0.387	>7.727	0
M6554	55387.274298	>17.072	14.688 ± 0.237	>10.711	7.375 ± 0.367	0
M6554	55387.406602	>17.026	>15.627	10.396 ± 0.228	>7.706	0
M6554	55387.803386	>17.049	15.149 ± 0.365	10.767 ± 0.321	>7.198	0
M6554	55387.803513	>16.527	>15.521	10.429 ± 0.233	>7.700	0
N0549	55213.307566	16.328 ± 0.290	14.227 ± 0.173	8.375 ± 0.040	6.201 ± 0.127	0
N0549	55213.439998	15.747 ± 0.186	13.509 ± 0.101	8.018 ± 0.035	5.806 ± 0.094	0
N0549	55213.506087	16.799 ± 0.434	14.208 ± 0.169	8.320 ± 0.039	6.157 ± 0.110	0
N0549	55213.572303	15.969 ± 0.221	13.807 ± 0.134	8.185 ± 0.036	6.283 ± 0.125	0
N0549	55213.638519	16.095 ± 0.235	13.792 ± 0.134	8.258 ± 0.041	6.021 ± 0.111	0
N0549	55213.770951	15.813 ± 0.178	13.267 ± 0.078	7.899 ± 0.031	5.875 ± 0.089	0
N4145	55276.662954	14.682 ± 0.145	11.154 ± 0.027	6.172 ± 0.015	4.179 ± 0.032	0
N4145	55276.729043	11.760 ± 0.021	10.817 ± 0.026	6.680 ± 0.025	4.465 ± 0.050	0
O7517	55405.053303	15.460 ± 0.140	13.243 ± 0.068	7.717 ± 0.026	5.443 ± 0.060	0
O7517	55405.119519	15.423 ± 0.142	9.734 ± 0.009	7.927 ± 0.031	5.837 ± 0.083	0
O7517	55405.185607	16.315 ± 0.312	13.888 ± 0.123	8.056 ± 0.033	5.926 ± 0.098	0
O7517	55405.251695	16.410 ± 0.302	14.083 ± 0.128	7.922 ± 0.027	5.791 ± 0.114	0
Q4357	55543.555716	16.689 ± 0.399	14.680 ± 0.259	–	–	0
Q4357	55543.820325	16.880 ± 0.474	14.565 ± 0.256	–	–	0
Q4357	55543.886414	>16.733	14.489 ± 0.232	–	–	0
Q4357	55543.952502	16.812 ± 0.474	14.326 ± 0.224	–	–	0
Q4357	55544.151022	16.689 ± 0.387	14.485 ± 0.207	–	–	0
W3179	55332.780675	12.511 ± 0.027	10.264 ± 0.021	5.138 ± 0.013	3.186 ± 0.032	0
W3179	55332.847018	13.656 ± 0.047	10.448 ± 0.020	5.116 ± 0.015	3.136 ± 0.033	0
J94C00B	55393.643342	15.560 ± 0.188	14.105 ± 0.168	8.835 ± 0.052	7.039 ± 0.237	0
J94C00B	55393.775646	16.355 ± 0.392	14.469 ± 0.192	9.203 ± 0.078	7.080 ± 0.281	0
J94C00B	55393.841862	15.908 ± 0.199	14.145 ± 0.150	8.837 ± 0.056	6.730 ± 0.173	0
J94C00B	55393.974166	15.303 ± 0.200	14.453 ± 0.232	8.969 ± 0.065	6.985 ± 0.247	0
J94C00B	55394.040254	14.479 ± 0.078	14.054 ± 0.169	9.025 ± 0.061	6.466 ± 0.144	0
J94C00B	55394.238773	>16.131	15.034 ± 0.337	8.908 ± 0.054	6.755 ± 0.178	0
J98K03N	55260.749926	12.270 ± 0.026	9.421 ± 0.020	4.826 ± 0.014	3.156 ± 0.026	0
J98W02B	55292.050593	16.337 ± 0.305	13.985 ± 0.130	8.107 ± 0.032	6.323 ± 0.140	0
J98W02B	55292.116808	16.483 ± 0.403	14.078 ± 0.145	8.246 ± 0.038	6.232 ± 0.129	0
J99XD6K	55542.071462	14.141 ± 0.058	11.241 ± 0.026	–	–	0
K00A06A	55403.870464	13.560 ± 0.041	10.367 ± 0.022	5.193 ± 0.014	3.271 ± 0.023	0
K00A06A	55403.870591	13.554 ± 0.042	10.371 ± 0.027	5.225 ± 0.014	3.316 ± 0.032	0
K00A06C	55525.179159	16.414 ± 0.331	13.736 ± 0.116	–	–	0
K00A06C	55525.245375	16.965 ± 0.490	13.646 ± 0.104	–	–	0
K00A06C	55525.311463	16.479 ± 0.317	13.530 ± 0.090	–	–	0
K00A06C	55525.377551	15.894 ± 0.193	13.640 ± 0.101	–	–	0
K00A06C	55525.377551	15.894 ± 0.193	13.640 ± 0.101	–	–	0
K00R52E	55269.275193	15.638 ± 0.144	12.815 ± 0.055	7.329 ± 0.019	5.542 ± 0.058	0
K00R52E	55269.341408	16.020 ± 0.206	13.452 ± 0.080	7.559 ± 0.023	5.651 ± 0.083	0
K00R52E	55269.407497	>17.108	13.699 ± 0.100	7.970 ± 0.026	6.018 ± 0.117	0
K02B25F	55393.366511	15.824 ± 0.213	12.907 ± 0.070	7.008 ± 0.021	4.928 ± 0.043	0
K02B25F	55393.366638	15.831 ± 0.187	12.801 ± 0.062	7.019 ± 0.019	4.981 ± 0.053	0
K02JA0R	55316.413042	>16.829	>15.589	10.043 ± 0.128	7.732 ± 0.457	0
K02X38Y	55251.356346	15.556 ± 0.192	12.894 ± 0.078	7.673 ± 0.026	5.920 ± 0.097	0
K02X38Y	55251.422434	16.038 ± 0.256	13.548 ± 0.144	8.000 ± 0.034	6.244 ± 0.124	0
K02X38Y	55251.422562	16.597 ± 0.448	13.612 ± 0.131	7.949 ± 0.034	6.078 ± 0.121	0
K03U11V	55499.353352	10.816 ± 0.020	7.966 ± 0.019	–	–	0
K04F11G	55295.775994	15.355 ± 0.140	12.881 ± 0.054	7.733 ± 0.026	5.768 ± 0.077	0
K04F11G	55295.776121	15.588 ± 0.208	12.841 ± 0.057	7.720 ± 0.027	5.655 ± 0.082	0
K04K17H	55359.062532	16.962 ± 0.516	14.314 ± 0.182	8.427 ± 0.042	6.464 ± 0.154	0
K04K17H	55359.12862	>16.453	13.902 ± 0.115	8.537 ± 0.044	6.653 ± 0.181	0
K04K17H	55359.194708	>15.533	13.872 ± 0.122	8.260 ± 0.038	6.450 ± 0.163	0
K04K17H	55359.260797	>16.426	13.637 ± 0.096	8.063 ± 0.034	6.265 ± 0.124	0
K04K17H	55359.260924	>16.571	13.719 ± 0.116	8.144 ± 0.037	6.152 ± 0.124	0
K04K17H	55359.3931	>16.406	14.569 ± 0.203	8.451 ± 0.043	6.567 ± 0.176	0
K04S56C	55416.036814	>16.635	>15.048	9.756 ± 0.122	–	0
K04S56C	55416.16899	13.643 ± 0.062	13.425 ± 0.094	10.840 ± 0.372	–	0
K04S56C	55416.367382	16.373 ± 0.413	>15.258	10.356 ± 0.222	–	0
K04S56C	55416.367382	15.689 ± 0.206	>15.384	10.495 ± 0.254	–	0

Table 1—Continued

Name	MJD	W1 (mag)	W2 (mag)	W3 (mag)	W4 (mag)	Aperture
K05GC0C	55532.148373	13.180 ± 0.038	10.531 ± 0.024	–	–	0
K05U00O	55265.148428	>17.014	14.885 ± 0.265	9.463 ± 0.098	7.619 ± 0.456	0
K05U00O	55265.214644	>16.971	15.190 ± 0.390	9.507 ± 0.104	>6.858	0
K05X01B	55305.354108	>17.074	>15.772	10.651 ± 0.262	>7.230	0
K05X01B	55305.420196	>17.229	>15.407	10.504 ± 0.210	7.341 ± 0.327	0
K05X01B	55305.486412	>17.113	>14.983	10.437 ± 0.214	>7.641	0
K05X01B	55305.5525	>16.888	>14.939	10.695 ± 0.257	>7.978	0
K07E00F	55256.742863	15.018 ± 0.129	11.903 ± 0.034	6.476 ± 0.017	4.648 ± 0.044	0
K07E00F	55256.808952	14.948 ± 0.098	11.836 ± 0.032	6.446 ± 0.017	4.588 ± 0.033	0
K08N03P	55398.084496	16.307 ± 0.331	12.470 ± 0.052	7.210 ± 0.019	5.198 ± 0.055	0
K08N03P	55398.150584	16.095 ± 0.256	12.847 ± 0.065	7.480 ± 0.023	5.503 ± 0.070	0
K08X00M	55214.618135	15.190 ± 0.107	12.786 ± 0.056	6.877 ± 0.020	4.922 ± 0.182	0
K08X00M	55214.618262	15.185 ± 0.109	12.737 ± 0.052	6.928 ± 0.018	4.768 ± 0.128	0
K09B00D*	55360.417023	>16.738	>15.505	>11.776	>7.587	11, 11, 11, 12
K09F00D	55493.292455	14.786 ± 0.082	11.401 ± 0.036	–	–	0
K09F00D	55493.358543	15.101 ± 0.105	11.453 ± 0.032	–	–	0
K09F00D	55493.358671	14.893 ± 0.096	11.408 ± 0.031	–	–	0
K09F04Y	55245.376313	>15.811	15.222 ± 0.419	9.254 ± 0.087	7.373 ± 0.368	0
K09U19Y	55278.763519	>17.235	14.870 ± 0.271	9.418 ± 0.082	7.533 ± 0.346	0
K09U19Y	55278.895824	>16.511	>15.076	9.405 ± 0.079	7.774 ± 0.441	0
K09U19Y	55279.689648	>17.143	15.374 ± 0.406	9.263 ± 0.068	7.098 ± 0.230	0
K09U19Y	55279.689775	>16.527	15.212 ± 0.333	9.248 ± 0.073	6.444 ± 0.134	0
K09U19Y	55279.821952	>16.501	15.004 ± 0.288	9.188 ± 0.067	7.033 ± 0.220	0
K09U19Y	55279.822079	>16.702	14.555 ± 0.203	9.230 ± 0.072	7.358 ± 0.309	0
K09U19Y	55279.954383	>16.442	15.162 ± 0.337	9.189 ± 0.065	6.978 ± 0.242	0
K09U19Y	55280.218991	>16.082	14.538 ± 0.181	9.182 ± 0.067	7.726 ± 0.432	0
K09U19Y	55280.351295	>16.632	14.727 ± 0.215	9.378 ± 0.080	7.044 ± 0.222	0
K09U19Y	55280.748209	>16.964	15.407 ± 0.400	9.237 ± 0.071	7.537 ± 0.355	0
K09U19Y	55280.880513	>16.555	14.721 ± 0.238	9.188 ± 0.068	7.192 ± 0.266	0
K09U19Y	55281.012817	>17.067	14.691 ± 0.211	9.159 ± 0.065	7.079 ± 0.255	0
K09U19Y	55281.145121	16.812 ± 0.414	14.512 ± 0.180	9.191 ± 0.072	6.953 ± 0.219	0
K09U19Y	55281.277425	16.580 ± 0.420	14.732 ± 0.227	9.070 ± 0.061	>7.336	0
K09U19Y	55281.542034	>17.217	15.122 ± 0.303	9.308 ± 0.077	7.120 ± 0.265	0
K09U19Y	55281.674338	>17.046	14.963 ± 0.277	9.359 ± 0.079	7.065 ± 0.234	0
K09U19Y	55281.806642	>17.167	15.254 ± 0.395	9.310 ± 0.076	6.602 ± 0.154	0
K09U19Y	55281.938946	>16.666	15.011 ± 0.259	9.318 ± 0.076	6.804 ± 0.188	0
K09U19Y	55281.939073	16.850 ± 0.439	14.908 ± 0.241	9.333 ± 0.075	6.835 ± 0.196	0
K09U19Y	55282.071125	16.503 ± 0.318	14.572 ± 0.198	9.186 ± 0.068	6.891 ± 0.202	0
K09U19Y	55282.071377	>17.038	15.316 ± 0.396	9.128 ± 0.064	7.006 ± 0.220	0
K09U19Y	55282.335985	14.923 ± 0.095	13.620 ± 0.088	8.926 ± 0.054	6.706 ± 0.198	0
K09U19Y	55282.600593	>16.455	14.354 ± 0.154	–	–	0
K09U19Y	55282.732897	>17.212	14.941 ± 0.251	8.945 ± 0.054	6.911 ± 0.220	0
K10A02N	55244.206332	>16.811	14.802 ± 0.229	9.884 ± 0.133	>7.847	0
K10A02N	55244.338636	>17.032	14.822 ± 0.255	9.873 ± 0.132	>7.496	0
K10A02N	55244.404724	>16.554	15.125 ± 0.324	10.055 ± 0.156	7.659 ± 0.450	0
K10A02N	55244.537028	>16.716	15.603 ± 0.519	10.006 ± 0.136	>7.672	0
K10A30E	55214.760372	>17.101	15.572 ± 0.515	9.608 ± 0.095	7.778 ± 0.494	0
K10A30E	55214.760372	>16.228	>15.693	9.971 ± 0.177	>7.345	0
K10A30E	55214.760372	>17.152	>15.588	10.732 ± 0.275	>7.461	0
K10A40G	55220.615821	15.638 ± 0.151	12.708 ± 0.058	7.519 ± 0.024	5.759 ± 0.078	0
K10B00C	55221.475481	14.694 ± 0.075	12.457 ± 0.045	6.435 ± 0.016	4.497 ± 0.037	0
K10B02K	55216.413863	16.131 ± 0.248	13.081 ± 0.065	7.304 ± 0.022	5.268 ± 0.051	0
K10C01K	55252.229502	16.686 ± 0.377	>15.159	10.294 ± 0.169	>7.384	0
K10C01K	55252.229629	>16.508	>14.927	10.397 ± 0.192	>7.519	0
K10C01K	55252.229502	16.686 ± 0.377	>15.159	10.294 ± 0.169	>7.384	0
K10C19C	55247.394099	>16.478	14.248 ± 0.158	9.296 ± 0.091	7.454 ± 0.353	0
K10C19C	55247.394226	>16.830	14.356 ± 0.173	9.226 ± 0.075	7.301 ± 0.319	0
K10C19C	55247.460315	>16.600	14.481 ± 0.229	9.225 ± 0.081	7.758 ± 0.498	0
K10C19F	55225.611168	>17.173	15.114 ± 0.438	10.664 ± 0.244	>7.254	0
K10C19F	55225.677384	16.800 ± 0.470	15.251 ± 0.370	10.645 ± 0.234	>7.382	0
K10C19F	55225.7436	>17.204	15.669 ± 0.495	10.035 ± 0.147	>7.374	0
K10C44O	55220.21114	>17.200	>15.141	10.278 ± 0.193	>7.922	0
K10C55D	55251.619171	15.958 ± 0.254	13.434 ± 0.116	8.073 ± 0.032	6.334 ± 0.152	0
K10C55D	55251.68526	>16.906	14.267 ± 0.286	8.409 ± 0.048	6.725 ± 0.228	0
K10C55F	55272.262029	>16.712	14.721 ± 0.251	9.711 ± 0.115	>7.155	0
K10D00L	55224.83708	>16.476	13.903 ± 0.120	9.229 ± 0.077	>6.882	0
K10D00L	55224.903296	>16.299	13.521 ± 0.092	9.144 ± 0.079	>7.258	0

Table 1—Continued

Name	MJD	W1 (mag)	W2 (mag)	W3 (mag)	W4 (mag)	Aperture
K10D00O	55249.932962	16.739 ± 0.481	13.657 ± 0.103	7.925 ± 0.032	5.966 ± 0.105	0
K10D01F	55287.22576	>17.163	>15.668	10.142 ± 0.161	>7.320	0
K10D01F	55287.291976	>16.830	>15.321	10.440 ± 0.196	7.725 ± 0.496	0
K10D01F	55287.358064	>17.214	15.697 ± 0.538	10.666 ± 0.256	7.897 ± 0.514	0
K10D01F	55287.42428	>17.017	14.891 ± 0.290	10.490 ± 0.221	7.873 ± 0.505	0
K10D01F	55287.490496	>16.888	>15.135	10.214 ± 0.162	7.728 ± 0.476	0
K10D01F	55287.556584	>17.143	>15.007	10.832 ± 0.293	>7.326	0
K10D01X	55238.600531	15.791 ± 0.171	13.216 ± 0.068	8.210 ± 0.032	6.161 ± 0.109	0
K10D01X	55238.600658	15.832 ± 0.199	13.115 ± 0.066	8.381 ± 0.042	6.314 ± 0.142	0
K10D01X	55238.666746	>16.330	13.737 ± 0.108	8.565 ± 0.044	6.411 ± 0.131	0
K10E21G*	55296.4873036	>17.061	>13.603	11.586 ± 0.161	>7.682	11, 11, 11, 12
K10E43C	55282.188656	>17.014	>15.274	9.976 ± 0.158	>7.219	0
K10E43C	55282.585568	>17.018	>15.498	–	7.165 ± 0.281	0
K10E43C	55282.651784	>16.900	>15.235	10.709 ± 0.346	>7.158	0
K10E43C	55282.784088	>16.960	>15.462	10.613 ± 0.276	>6.939	0
K10E43K	55254.097037	>16.463	14.365 ± 0.181	8.700 ± 0.052	6.621 ± 0.185	0
K10E43K	55254.163125	16.566 ± 0.341	14.107 ± 0.139	8.708 ± 0.053	6.765 ± 0.224	0
K10F00C*	55306.8863662	>17.061	>13.603	12.254 ± 0.175	>8.253	11, 11, 11, 12
K10F00K*	55293.0473	>17.061	>13.603	11.422 ± 0.133	>7.762	11, 11, 11, 12
K10F00S	55271.941138	>16.908	>15.191	9.927 ± 0.135	>7.898	0
K10F00S	55272.007226	>17.171	>15.792	9.767 ± 0.115	>7.273	0
K10F00S	55272.007353	>17.060	>15.696	9.981 ± 0.143	>7.149	0
K10F00T	55280.951568	>16.639	>15.228	8.881 ± 0.051	6.377 ± 0.130	0
K10F06D	55267.728293	16.184 ± 0.268	15.167 ± 0.345	8.717 ± 0.053	6.713 ± 0.181	0
K10F06D	55267.72842	>16.968	>14.921	8.612 ± 0.049	6.391 ± 0.160	0
K10F07D	55302.871016	>16.552	14.559 ± 0.188	8.576 ± 0.044	6.666 ± 0.184	0
K10F07D	55302.937232	>16.507	14.730 ± 0.235	8.687 ± 0.046	6.747 ± 0.173	0
K10F07E	55241.261768	>17.031	>15.039	9.726 ± 0.118	7.340 ± 0.339	0
K10F07E	55241.327983	>17.161	15.454 ± 0.487	9.326 ± 0.083	>7.238	0
K10F09R	55288.3173	>17.117	>15.582	10.326 ± 0.194	>7.471	0
K10F09R	55288.383389	>17.150	>15.178	10.276 ± 0.182	>7.332	0
K10F09W	55282.31905	15.821 ± 0.214	13.149 ± 0.072	8.357 ± 0.039	6.496 ± 0.158	0
K10F09W	55282.319177	15.122 ± 0.146	13.109 ± 0.092	8.212 ± 0.039	6.381 ± 0.157	0
K10F09X	55272.489454	>17.159	>15.787	10.673 ± 0.255	7.103 ± 0.243	0
K10F10F	55318.265811	>17.157	14.946 ± 0.300	9.399 ± 0.079	7.992 ± 0.513	0
K10G05Z	55307.946455	>16.446	14.622 ± 0.200	8.574 ± 0.043	6.244 ± 0.120	0
K10G06B*	55261.791	>16.927	>15.794	11.888 ± 0.235	>7.973	11, 11, 11, 12
K10G06T	55318.700544	>17.166	15.292 ± 0.366	10.456 ± 0.205	7.824 ± 0.463	0
K10G06T	55318.700671	>17.247	15.609 ± 0.526	10.462 ± 0.222	>7.390	0
K10G06T	55318.766676	>17.089	14.897 ± 0.276	9.825 ± 0.121	>7.573	0
K10G06U	55321.642434	>16.454	14.069 ± 0.189	8.378 ± 0.055	6.088 ± 0.150	0
K10G06U	55321.70865	>16.679	14.664 ± 0.291	8.380 ± 0.047	6.455 ± 0.158	0
K10G06U	55321.774738	>16.315	13.743 ± 0.115	8.329 ± 0.038	6.486 ± 0.191	0
K10G07H	55288.141829	>16.582	14.325 ± 0.183	8.567 ± 0.046	6.380 ± 0.153	0
K10G23L	55273.164982	>16.997	>15.638	11.493 ± 0.523	>7.641	0
K10G23L	55273.164982	>16.939	>15.625	9.989 ± 0.143	>7.388	0
K10G23L	55273.231197	>16.915	15.398 ± 0.414	10.253 ± 0.174	>7.152	0
K10G23L	55273.231197	13.837 ± 0.055	13.993 ± 0.124	>10.847	>7.775	0
K10G23L	55273.297286	>16.793	>15.526	9.979 ± 0.135	>7.598	0
K10G23L	55273.297286	13.154 ± 0.037	13.087 ± 0.067	>11.496	>7.975	0
K10G23L	55273.363501	14.061 ± 0.058	13.951 ± 0.125	10.667 ± 0.264	>7.793	0
K10G23L	55273.363501	11.909 ± 0.025	11.984 ± 0.036	11.300 ± 0.462	>7.965	0
K10G23L	55273.363501	15.795 ± 0.186	>14.787	>11.463	>7.669	0
K10G23M	55299.095057	16.852 ± 0.479	12.864 ± 0.060	6.363 ± 0.017	4.285 ± 0.033	0
K10G23X	55282.677505	>17.093	14.521 ± 0.218	8.477 ± 0.041	6.404 ± 0.134	0
K10G23X	55282.743721	>16.873	14.644 ± 0.240	8.511 ± 0.048	6.427 ± 0.151	0
K10G24A	55330.6605	14.919 ± 0.090	12.578 ± 0.047	7.599 ± 0.023	5.722 ± 0.077	0
K10G24A	55330.726716	15.176 ± 0.102	12.702 ± 0.049	7.646 ± 0.023	5.635 ± 0.076	0
K10H00A	55285.077825	>17.064	>15.007	10.495 ± 0.208	>7.507	0
K10H20V	55319.519836	15.660 ± 0.151	12.061 ± 0.036	6.381 ± 0.019	4.535 ± 0.032	0
K10H20V	55319.519964	15.833 ± 0.176	11.990 ± 0.037	6.415 ± 0.015	4.550 ± 0.035	0
K10H20V	55319.586052	14.486 ± 0.069	11.294 ± 0.026	6.238 ± 0.013	4.542 ± 0.123	0
K10J03H	55328.677603	>17.081	15.557 ± 0.421	9.483 ± 0.088	7.270 ± 0.275	0
K10J03J	55305.935151	>17.097	15.331 ± 0.454	9.090 ± 0.066	7.251 ± 0.342	0
K10J03J	55306.001239	>16.496	14.761 ± 0.246	9.230 ± 0.081	7.106 ± 0.250	0
K10J34V	55341.608746	14.392 ± 0.063	11.585 ± 0.027	6.261 ± 0.014	4.168 ± 0.031	0
K10J39W	55307.8032	>16.769	>15.647	10.610 ± 0.239	>7.988	0



Table 1—Continued

Name	MJD	W1 (mag)	W2 (mag)	W3 (mag)	W4 (mag)	Aperture
K10J39W	55307.869416	>16.657	>15.377	10.324 ± 0.208	>7.250	0
K10J41L	55335.655835	>16.305	13.066 ± 0.059	7.537 ± 0.022	5.485 ± 0.061	0
K10J41L	55335.721924	16.795 ± 0.403	13.748 ± 0.103	7.949 ± 0.028	5.786 ± 0.073	0
K10J71O	55343.927944	>16.688	>15.660	10.462 ± 0.202	>7.427	0
K10K07V	55341.066415	>16.441	15.270 ± 0.498	10.240 ± 0.200	7.521 ± 0.403	0
K10K07V	55341.132631	>17.066	15.266 ± 0.430	10.348 ± 0.214	7.123 ± 0.320	0
K10K08A	55305.657172	>16.512	14.148 ± 0.139	8.721 ± 0.051	6.624 ± 0.172	0
K10K08A	55305.789476	15.988 ± 0.206	14.027 ± 0.140	8.820 ± 0.048	6.416 ± 0.148	0
K10K10P	55302.942835	>17.152	>15.425	10.511 ± 0.198	7.632 ± 0.370	0
K10K10P	55303.009051	>17.211	>15.776	11.151 ± 0.340	>7.586	0
K10K10P	55303.009051	16.011 ± 0.204	15.407 ± 0.416	>11.233	7.098 ± 0.260	0
K10K10P	55303.207443	15.800 ± 0.175	14.804 ± 0.226	>11.111	>7.276	0
K10K10P	55303.273659	>16.880	>15.467	10.368 ± 0.186	7.231 ± 0.297	0
K10K10P	55303.538267	>16.984	15.272 ± 0.330	10.359 ± 0.182	>7.632	0
K10L34K	55363.962739	>17.273	15.292 ± 0.382	9.510 ± 0.084	6.959 ± 0.236	0
K10L34K	55364.028828	>16.940	15.264 ± 0.355	9.146 ± 0.069	6.873 ± 0.195	0
K10L34K	55364.028955	>17.104	>15.645	9.130 ± 0.069	6.969 ± 0.231	0
K10L61K	55344.064577	>17.003	14.878 ± 0.261	9.004 ± 0.058	6.900 ± 0.252	0
K10L61K	55344.130665	16.252 ± 0.321	15.338 ± 0.372	9.314 ± 0.084	7.026 ± 0.219	0
K10L61K	55344.130793	15.474 ± 0.143	14.273 ± 0.199	9.302 ± 0.071	7.803 ± 0.512	0
K10L61K	55344.196881	>17.073	>15.640	9.235 ± 0.071	6.921 ± 0.262	0
K10L61K	55344.262969	>17.049	>15.141	9.218 ± 0.068	7.788 ± 0.459	0
K10L63Z	55374.316813	13.701 ± 0.045	10.485 ± 0.024	5.564 ± 0.012	3.634 ± 0.047	0
K10L63Z	55374.382901	13.626 ± 0.041	10.432 ± 0.023	5.486 ± 0.011	3.551 ± 0.026	0
K10L64B*	55381.0071	>16.588	>15.548	11.382 ± 0.135	>7.747	11, 11, 11, 12
K10M01G	55383.93678	>17.192	>14.858	10.054 ± 0.154	7.681 ± 0.469	0
K10M01G	55384.002996	>17.181	>15.163	10.422 ± 0.202	>7.130	0
K10M01G	55384.069211	>17.141	>15.594	10.175 ± 0.166	7.526 ± 0.392	0
K10M01G	55384.135299	>17.196	>15.096	10.256 ± 0.203	>7.701	0
K10M01G	55384.26773	>17.125	>15.074	10.464 ± 0.211	>7.595	0
K10M01P	55360.337436	16.862 ± 0.479	>15.724	8.502 ± 0.039	6.079 ± 0.093	0
K10M01P	55360.403525	>15.920	>15.576	8.769 ± 0.048	6.655 ± 0.181	0
K10M01Y	55372.696314	>16.615	14.617 ± 0.206	8.654 ± 0.043	6.658 ± 0.166	0
K10M01Y	55372.76253	16.335 ± 0.266	>15.636	8.769 ± 0.046	6.948 ± 0.226	0
K10M01Y	55372.828618	16.262 ± 0.274	14.392 ± 0.172	8.564 ± 0.041	6.624 ± 0.157	0
K10M01Y	55372.894706	>16.486	15.195 ± 0.359	9.006 ± 0.059	6.840 ± 0.203	0
K10N00A	55381.237224	16.273 ± 0.271	13.678 ± 0.095	7.745 ± 0.026	5.711 ± 0.078	0
K10N01K	55382.945966	13.523 ± 0.039	10.452 ± 0.023	5.488 ± 0.011	3.512 ± 0.030	0
K10N01K	55383.012182	13.558 ± 0.041	10.422 ± 0.024	5.470 ± 0.016	3.563 ± 0.035	0
K10N01K	55383.144485	13.534 ± 0.047	10.396 ± 0.020	5.470 ± 0.018	3.541 ± 0.020	0
K10O01A	55398.91461	16.421 ± 0.383	13.596 ± 0.102	8.251 ± 0.038	6.915 ± 0.267	0
K10O01A	55398.980825	15.899 ± 0.196	13.627 ± 0.104	8.334 ± 0.041	6.391 ± 0.162	0
K10P09K	55395.805917	16.739 ± 0.438	14.737 ± 0.270	9.843 ± 0.146	>7.050	0
K10P09K	55395.93822	16.515 ± 0.379	14.325 ± 0.179	9.119 ± 0.081	7.301 ± 0.350	0
K10P09K	55396.004309	>16.592	14.660 ± 0.222	9.487 ± 0.109	>7.048	0
K10P09K	55396.004436	16.877 ± 0.500	14.928 ± 0.307	9.321 ± 0.089	7.189 ± 0.307	0
K10P66R	55303.619254	>17.055	>15.662	10.442 ± 0.229	>7.579	0
K10P66R	55304.016167	>16.998	>15.731	10.740 ± 0.310	>7.769	0
K10P66R	55304.148471	14.998 ± 0.097	15.151 ± 0.313	>11.172	>7.563	0
K10P66R	55304.148599	15.248 ± 0.123	14.869 ± 0.252	10.897 ± 0.306	>7.793	0
K10P66R	55304.280903	>16.998	>15.254	10.344 ± 0.191	7.164 ± 0.266	0
K10P66R	55304.346991	>17.147	>15.614	10.427 ± 0.223	>7.836	0
K10P66R	55304.413207	>16.841	>15.133	10.232 ± 0.175	>7.867	0
K10P66R	55304.6116	>17.133	>15.428	10.468 ± 0.214	>7.867	0
K10P66R	55304.743904	>17.045	>14.979	10.479 ± 0.220	>7.645	0
K10P66R	55308.250156	>16.568	15.019 ± 0.390	10.197 ± 0.180	>7.602	0
K10P66R	55399.411991	11.734 ± 0.022	8.794 ± 0.018	3.289 ± 0.015	1.475 ± 0.017	0
K10P66R	55303.619254	>17.055	>15.662	10.442 ± 0.229	>7.579	0
K10P66R	55304.016167	>16.998	>15.731	10.740 ± 0.310	>7.769	0
K10P66R	55304.148471	14.998 ± 0.097	15.151 ± 0.313	>11.172	>7.563	0
K10P66R	55304.148599	15.248 ± 0.123	14.869 ± 0.252	10.897 ± 0.306	>7.793	0
K10P66R	55304.280903	>16.998	>15.254	10.344 ± 0.191	7.164 ± 0.266	0
K10P66R	55304.346991	>17.147	>15.614	10.427 ± 0.223	>7.836	0
K10P66R	55304.413207	>16.841	>15.133	10.232 ± 0.175	>7.867	0
K10P66R	55304.6116	>17.133	>15.428	10.468 ± 0.214	>7.867	0
K10P66R	55304.743904	>17.045	>14.979	10.479 ± 0.220	>7.645	0
K10P66R	55308.250156	>16.568	15.019 ± 0.390	10.197 ± 0.180	>7.602	0

Table 1—Continued

Name	MJD	W1 (mag)	W2 (mag)	W3 (mag)	W4 (mag)	Aperture
K10P66R	55399.411991	11.734 ± 0.022	8.794 ± 0.018	3.289 ± 0.015	1.475 ± 0.017	0
K10Q02G	55442.835858	16.537 ± 0.418	12.840 ± 0.105	>8.231	–	0
K10R53J	55446.26074	15.112 ± 0.117	11.506 ± 0.030	6.060 ± 0.063	–	0
K10T04N	55468.515321	>17.061	13.603 ± 0.105	>8.338	–	0
K10TE9U	55498.588434	15.247 ± 0.163	12.164 ± 0.054	–	–	0
K10U07C	55503.081294	16.543 ± 0.334	12.574 ± 0.058	–	–	0
K10V11T	55502.789563	16.112 ± 0.277	13.413 ± 0.084	–	–	0
K10V11T	55502.855652	15.868 ± 0.196	13.248 ± 0.072	–	–	0
K10V72D	55512.768409	15.951 ± 0.329	12.658 ± 0.054	–	–	0
K10V72D	55512.834497	15.294 ± 0.128	12.856 ± 0.063	–	–	0
K10V72D	55512.966674	15.962 ± 0.230	12.853 ± 0.065	–	–	0
K10V72D	55514.288315	15.823 ± 0.187	13.017 ± 0.076	–	–	0
K10VD9K	55511.208514	>16.587	14.830 ± 0.281	–	–	0
K10VD9K	55511.274602	16.094 ± 0.220	14.143 ± 0.139	–	–	0
K10VD9K	55511.274729	>16.534	14.486 ± 0.189	–	–	0
K10VD9K	55511.340818	16.511 ± 0.320	14.446 ± 0.174	–	–	0
K10W00B	55512.114019	14.332 ± 0.064	11.404 ± 0.027	–	–	0
K10Y00D	55566.173782	>16.983	14.356 ± 0.240	–	–	0
K11A55V	55571.253941	16.601 ± 0.345	13.365 ± 0.086	–	–	0
K11A55V	55571.320157	16.208 ± 0.315	13.321 ± 0.080	–	–	0
K11A55V	55571.386372	16.075 ± 0.223	13.523 ± 0.094	–	–	0

Table 2. Thermal fit results for the 106 new NEO detections reported in this work. This table contains the preliminary thermal fit results based on the first-pass version of the WISE data processing as described in the text. The columns contain object name,  $H$  magnitude, phase curve slope parameter  $G$ , diameter, visible albedo  $p_V$ , beaming parameter  $\eta$ , infrared albedo  $p_{IR}$ , and number of observations in each of the four WISE bands. The  $1 - \sigma$  errors presented here were statistically generated using Monte Carlo modeling. WISE fluxes, absolute magnitude  $H$ , and  $G$  were varied by their  $1 - \sigma$  error bars, as well as beaming ( $\eta$ ) and  $p_{IR}$  when these two parameters could not be fit. The quoted precision for each parameter follows the object with the most significant figures for the error on that value in the table. The statistical errors on diameter and  $p_V$  for each object in the table should be added in quadrature to the systematic errors described in the text and discussed in Mainzer et al. (2011c). If  $\eta = \pi$ , the FRM was used instead of NEATM. Objects with multiple entries were observed at multiple epochs, which were fit separately.

Object	$H$	$G$	$D$ (km)	$p_V$	$\eta$	$p_{IR}$
85989	17.10	0.15	1.834 ± 0.018	0.076 ± 0.017	1.674 ± 0.025	0.072 ± 0.027
85989	17.10	0.15	1.853 ± 0.077	0.074 ± 0.018	2.001 ± 0.151	0.994 ± 0.110
88254	17.60	0.15	0.800 ± 0.012	0.252 ± 0.035	1.309 ± 0.046	0.352 ± 0.150
D7032	16.60	0.15	1.055 ± 0.322	0.183 ± 0.325	2.000 ± 0.500	0.310 ± 0.288
F2742	19.10	0.15	0.413 ± 0.005	0.264 ± 0.011	1.400 ± 0.500	0.276 ± 0.086
F4590	21.70	0.15	0.086 ± 0.002	0.530 ± 0.076	1.400 ± 0.500	0.848 ± 0.114
M6554	19.50	0.15	0.482 ± 0.007	0.125 ± 0.024	3.055 ± 0.060	0.200 ± 0.038
N0549	20.60	0.15	0.217 ± 0.004	0.216 ± 0.046	2.402 ± 0.072	0.346 ± 0.073
N4145	21.30	0.15	0.344 ± 0.006	0.045 ± 0.009	1.571 ± 0.044	0.010 ± 0.033
O7517	19.70	0.15	0.269 ± 0.005	0.357 ± 0.055	1.400 ± 0.500	0.929 ± 0.142
Q4357	21.00	0.15	0.439 ± 0.106	0.037 ± 0.024	2.000 ± 0.406	0.058 ± 0.039
W3179	18.20	0.15	1.170 ± 0.022	0.068 ± 0.013	1.970 ± 0.037	0.387 ± 0.177
J94C00B	21.00	0.15	0.193 ± 0.010	0.195 ± 0.026	2.124 ± 0.229	0.311 ± 0.042
J98K03N	18.40	0.15	1.060 ± 0.020	0.074 ± 0.014	1.165 ± 0.029	0.118 ± 0.022
J98W02B	21.80	0.15	0.150 ± 0.007	0.151 ± 0.034	2.790 ± 0.224	0.192 ± 0.429
J99XD6K	20.30	0.15	0.811 ± 0.403	0.020 ± 0.031	0.900 ± 0.390	0.032 ± 0.063
K00A06A	22.10	0.15	0.316 ± 0.005	0.026 ± 0.005	1.753 ± 0.034	0.085 ± 0.025
K00A06C	21.50	0.15	0.176 ± 0.005	0.143 ± 0.021	2.300 ± 0.500	0.316 ± 0.133
K00R52E	22.30	0.15	0.149 ± 0.005	0.095 ± 0.020	2.397 ± 0.150	0.230 ± 0.244
K02B25F	22.20	0.15	0.152 ± 0.003	0.100 ± 0.021	2.619 ± 0.111	0.101 ± 0.182
K02JA0R	24.30	0.15	0.028 ± 0.002	0.441 ± 0.110	3.000 ± 0.390	0.705 ± 0.145
K02X38Y	22.90	0.15	0.096 ± 0.003	0.134 ± 0.026	1.972 ± 0.113	0.130 ± 0.084
K03U11V	19.50	0.15	0.260 ± 0.003	0.376 ± 0.075	1.400 ± 0.500	0.601 ± 0.121
K04F11G	21.00	0.15	0.152 ± 0.003	0.306 ± 0.050	1.730 ± 0.067	0.415 ± 0.115
K04K17H	22.00	0.15	0.197 ± 0.011	0.072 ± 0.012	2.318 ± 0.224	0.115 ± 0.019
K04S56C	22.70	0.15	0.291 ± 0.042	0.017 ± 0.008	2.000 ± 0.514	0.028 ± 0.012
K05GC0C	19.60	0.15	0.906 ± 0.072	0.031 ± 0.006	0.755 ± 0.056	0.050 ± 0.009
K05U00O	22.10	0.15	0.164 ± 0.019	0.094 ± 0.028	2.303 ± 0.400	0.151 ± 0.045
K05X01B	22.00	0.15	0.099 ± 0.012	0.287 ± 0.099	2.000 ± 0.440	0.459 ± 0.158
K07E00F	21.40	0.15	0.260 ± 0.005	0.072 ± 0.013	2.062 ± 0.049	0.101 ± 0.034
K08N03P	23.30	0.15	0.193 ± 0.003	0.023 ± 0.004	1.993 ± 0.054	0.036 ± 0.006
K08X00M	19.90	0.15	0.367 ± 0.009	0.128 ± 0.032	2.989 ± 0.095	0.204 ± 0.051
K09F00D	22.10	0.15	0.472 ± 0.045	0.010 ± 0.003	2.421 ± 0.176	0.010 ± 0.003
K09F04Y	21.00	0.15	0.129 ± 0.013	0.421 ± 0.091	2.000 ± 0.366	0.673 ± 0.145
K09U19Y	23.40	0.15	0.105 ± 0.001	0.063 ± 0.012	1.400 ± 0.500	0.101 ± 0.019
K10A02N	22.20	0.15	0.123 ± 0.010	0.155 ± 0.035	1.600 ± 0.212	0.247 ± 0.055
K10A30E	23.60	0.15	0.050 ± 0.008	0.259 ± 0.147	2.000 ± 0.597	0.415 ± 0.198
K10A40G	22.10	0.15	0.089 ± 0.004	0.319 ± 0.053	1.803 ± 0.141	0.144 ± 0.119
K10B00C	22.20	0.15	0.080 ± 0.002	0.433 ± 0.034	1.400 ± 0.500	0.440 ± 0.125
K10B02K	22.00	0.15	0.118 ± 0.002	0.205 ± 0.043	1.400 ± 0.500	0.329 ± 0.069
K10C01K	24.00	0.15	0.084 ± 0.011	0.063 ± 0.024	2.000 ± 0.432	0.101 ± 0.038
K10C19C	22.30	0.15	0.104 ± 0.005	0.196 ± 0.032	1.724 ± 0.126	0.313 ± 0.052
K10C19F	21.90	0.15	0.083 ± 0.006	0.448 ± 0.111	2.400 ± 0.298	0.717 ± 0.144
K10C44O	24.60	0.15	0.034 ± 0.005	0.218 ± 0.102	2.000 ± 0.431	0.348 ± 0.151
K10C55D	23.10	0.15	0.083 ± 0.012	0.145 ± 0.034	2.009 ± 0.539	0.232 ± 0.055
K10C55F	21.70	0.15	0.176 ± 0.022	0.119 ± 0.031	2.000 ± 0.453	0.190 ± 0.050
K10D00L	27.00	0.15	0.019 ± 0.001	0.080 ± 0.018	1.102 ± 0.090	0.128 ± 0.029
K10D00O	21.70	0.15	0.149 ± 0.002	0.176 ± 0.036	1.400 ± 0.500	0.282 ± 0.058
K10D01F	21.90	0.15	0.159 ± 0.020	0.121 ± 0.060	2.000 ± 0.474	0.193 ± 0.097
K10D01X	21.60	0.15	0.167 ± 0.004	0.146 ± 0.023	1.606 ± 0.055	0.632 ± 0.164
K10E21G	24.40	0.15	0.090 ± 0.013	0.038 ± 0.016	2.000 ± 0.428	0.060 ± 0.025
K10E43C	23.00	0.15	0.051 ± 0.005	0.434 ± 0.095	2.400 ± 0.403	0.695 ± 0.127
K10E43K	21.70	0.15	0.233 ± 0.023	0.068 ± 0.014	2.346 ± 0.390	0.109 ± 0.023
K10F00C	24.00	0.15	0.093 ± 0.015	0.051 ± 0.017	2.000 ± 0.410	0.082 ± 0.027
K10F00K	23.80	0.15	0.087 ± 0.009	0.071 ± 0.020	2.000 ± 0.419	0.113 ± 0.032
K10F00S	24.50	0.15	0.023 ± 0.003	0.548 ± 0.164	2.000 ± 0.550	0.877 ± 0.156
K10F00T	25.70	0.15	0.018 ± 0.001	0.294 ± 0.062	1.400 ± 0.500	0.471 ± 0.099
K10F06D	26.80	0.15	0.008 ± 0.000	0.497 ± 0.081	1.400 ± 0.500	0.796 ± 0.117
K10F07D	22.10	0.15	0.075 ± 0.002	0.448 ± 0.070	1.400 ± 0.500	0.716 ± 0.112
K10F07E	23.70	0.15	0.045 ± 0.002	0.288 ± 0.043	1.400 ± 0.500	0.460 ± 0.068
K10F09R	26.10	0.15	0.015 ± 0.001	0.287 ± 0.053	1.400 ± 0.500	0.459 ± 0.085
K10F09W	26.70	0.15	0.024 ± 0.001	0.075 ± 0.014	1.226 ± 0.057	0.120 ± 0.022
K10F09X	24.20	0.15	0.030 ± 0.002	0.425 ± 0.068	3.142 ± 0.500	0.681 ± 0.109
K10F10F	21.70	0.15	0.095 ± 0.010	0.407 ± 0.093	2.000 ± 0.441	0.650 ± 0.146
K10G05Z	22.80	0.15	0.071 ± 0.002	0.281 ± 0.056	1.400 ± 0.500	0.450 ± 0.090
K10G06B	22.10	0.15	0.134 ± 0.021	0.142 ± 0.055	2.000 ± 0.433	0.227 ± 0.088
K10G06T	21.60	0.15	0.116 ± 0.015	0.300 ± 0.080	2.000 ± 0.470	0.480 ± 0.129

Table 2—Continued

Object	$H$	$G$	$D$ (km)	$p_V$	$\eta$	$PIR$
K10G06U	20.70	0.15	$0.252 \pm 0.022$	$0.147 \pm 0.030$	$2.336 \pm 0.335$	$0.235 \pm 0.048$
K10G07H	27.30	0.15	$0.008 \pm 0.000$	$0.326 \pm 0.043$	$1.400 \pm 0.500$	$0.521 \pm 0.069$
K10G23L	22.80	0.15	$0.092 \pm 0.014$	$0.159 \pm 0.099$	$2.000 \pm 0.557$	$0.255 \pm 0.155$
K10G23M	24.70	0.15	$0.341 \pm 0.000$	$0.010 \pm 0.000$	$0.860 \pm 0.500$	$0.010 \pm 0.000$
K10G23X	23.00	0.15	$0.060 \pm 0.001$	$0.334 \pm 0.051$	$1.400 \pm 0.500$	$0.535 \pm 0.081$
K10G24A	21.10	0.15	$0.150 \pm 0.005$	$0.285 \pm 0.080$	$1.532 \pm 0.110$	$0.708 \pm 0.202$
K10H00A	23.90	0.15	$0.032 \pm 0.004$	$0.482 \pm 0.130$	$2.100 \pm 0.357$	$0.772 \pm 0.141$
K10H20V	21.90	0.15	$0.465 \pm 0.007$	$0.016 \pm 0.003$	$1.912 \pm 0.035$	$0.025 \pm 0.005$
K10J03H	25.30	0.15	$0.039 \pm 0.005$	$0.087 \pm 0.026$	$2.000 \pm 0.414$	$0.139 \pm 0.042$
K10J03J	23.60	0.15	$0.032 \pm 0.001$	$0.609 \pm 0.076$	$1.400 \pm 0.500$	$0.678 \pm 0.273$
K10J34V	20.80	0.15	$0.226 \pm 0.005$	$0.165 \pm 0.041$	$1.988 \pm 0.080$	$0.239 \pm 0.069$
K10J39W	24.50	0.15	$0.039 \pm 0.005$	$0.187 \pm 0.063$	$2.000 \pm 0.511$	$0.300 \pm 0.100$
K10J41L	20.70	0.15	$0.359 \pm 0.023$	$0.073 \pm 0.014$	$2.382 \pm 0.255$	$0.117 \pm 0.022$
K10J71O	23.90	0.15	$0.037 \pm 0.004$	$0.349 \pm 0.114$	$2.000 \pm 0.440$	$0.558 \pm 0.182$
K10K07V	26.00	0.15	$0.013 \pm 0.001$	$0.397 \pm 0.070$	$1.400 \pm 0.500$	$0.635 \pm 0.112$
K10K08A	21.40	0.15	$0.183 \pm 0.019$	$0.147 \pm 0.034$	$2.298 \pm 0.487$	$0.235 \pm 0.054$
K10K10P	23.40	0.15	$0.087 \pm 0.010$	$0.101 \pm 0.036$	$2.000 \pm 0.390$	$0.161 \pm 0.057$
K10L34K	21.90	0.15	$0.108 \pm 0.002$	$0.271 \pm 0.048$	$1.400 \pm 0.500$	$0.434 \pm 0.078$
K10L61K	21.90	0.15	$0.191 \pm 0.019$	$0.084 \pm 0.022$	$2.221 \pm 0.420$	$0.135 \pm 0.035$
K10L63Z	20.10	0.15	$0.877 \pm 0.015$	$0.021 \pm 0.007$	$1.610 \pm 0.041$	$0.062 \pm 0.033$
K10L64B	21.70	0.15	$0.088 \pm 0.008$	$0.477 \pm 0.165$	$2.300 \pm 0.386$	$0.763 \pm 0.177$
K10M01G	23.30	0.15	$0.053 \pm 0.005$	$0.301 \pm 0.107$	$2.000 \pm 0.384$	$0.482 \pm 0.149$
K10M01P	21.40	0.15	$0.104 \pm 0.004$	$0.518 \pm 0.091$	$1.400 \pm 0.500$	$0.830 \pm 0.135$
K10M01Y	23.90	0.15	$0.043 \pm 0.001$	$0.265 \pm 0.029$	$1.400 \pm 0.500$	$0.424 \pm 0.046$
K10N00A	20.50	0.15	$0.320 \pm 0.011$	$0.109 \pm 0.026$	$2.862 \pm 0.191$	$0.144 \pm 0.426$
K10N01K	22.40	0.15	$0.219 \pm 0.002$	$0.040 \pm 0.006$	$1.624 \pm 0.025$	$0.109 \pm 0.031$
K10O01A	–	0.15	$0.663 \pm 0.035$	–	$2.058 \pm 0.186$	$0.418 \pm 0.274$
K10P09K	22.00	0.15	$0.143 \pm 0.008$	$0.138 \pm 0.040$	$1.798 \pm 0.159$	$0.220 \pm 0.064$
K10P66R	19.40	0.15	$0.695 \pm 0.018$	$0.063 \pm 0.012$	$1.992 \pm 0.046$	$0.178 \pm 0.044$
K10P66R	19.40	0.15	$0.488 \pm 0.061$	$0.129 \pm 0.041$	$2.000 \pm 0.463$	$0.362 \pm 0.115$
K10Q02G	24.30	0.15	$0.038 \pm 0.006$	$0.228 \pm 0.064$	$2.300 \pm 0.315$	$0.228 \pm 0.064$
K10R53J	24.00	0.15	$0.774 \pm 0.020$	$0.010 \pm 0.000$	$2.186 \pm 0.064$	$0.010 \pm 0.000$
K10T04N	27.36	0.15	$0.018 \pm 0.006$	$0.062 \pm 0.098$	$2.000 \pm 0.582$	$0.100 \pm 0.156$
K10TE9U	20.70	0.15	$0.603 \pm 0.195$	$0.025 \pm 0.015$	$1.388 \pm 0.374$	$0.041 \pm 0.025$
K10U07C	24.70	0.15	$0.043 \pm 0.011$	$0.129 \pm 0.066$	$2.000 \pm 0.461$	$0.206 \pm 0.105$
K10V11T	21.50	0.15	$0.152 \pm 0.044$	$0.189 \pm 0.162$	$2.000 \pm 0.500$	$0.302 \pm 0.209$
K10V72D	21.50	0.15	$0.124 \pm 0.005$	$0.290 \pm 0.035$	$1.400 \pm 0.500$	$0.434 \pm 0.150$
K10VD9K	23.70	0.15	$0.055 \pm 0.010$	$0.196 \pm 0.114$	$2.000 \pm 0.377$	$0.313 \pm 0.182$
K10W00B	24.10	0.15	$0.057 \pm 0.018$	$0.126 \pm 0.049$	$1.582 \pm 0.447$	$0.202 \pm 0.079$
K10Y00D	26.60	0.15	$0.026 \pm 0.009$	$0.060 \pm 0.068$	$2.000 \pm 0.602$	$0.096 \pm 0.108$
K11A55V	23.50	0.15	$0.063 \pm 0.024$	$0.176 \pm 0.156$	$1.128 \pm 0.415$	$0.282 \pm 0.193$